Carbohydrate Polymers 351 (2025) 123069

Contents lists available at ScienceDirect

Carbohydrate Polymers

journal homepage: www.elsevier.com/locate/carbpol

Combining antibacterial and wound healing features: Xanthan gum/guar gum 3D-printed scaffold tuned with hydroxypropyl-β-cyclodextrin/thymol and Zn^{2+}

Nicola Filippo Virzì [a,b], Patricia Diaz-Rodriguez [b], Angel Concheiro [b], Ana Otero [c], Antonino Mazzaglia [d], Valeria Pittalà [a,e,*], Carmen Alvarez-Lorenzo [b,**]

[a] Department of Drug and Health Science, University of Catania, Viale A. Doria 6, 95125 Catania, Italy
[b] Departamento de Farmacología, Farmacia y Tecnología Farmacéutica, I+D Farma (GI-1645), Faculty of Pharmacy, Instituto de Materiales (iMATUS), and Health Research Institute of Santiago de Compostela (IDIS), Universidade de Santiago de Compostela, 15782 Santiago de Compostela, Spain
[c] Departamento de Microbiología y Parasitología, Facultad de Biología, Edificio CiBUS and Aquatic One Health Research Center (ARCUS), Universidade de Santiago de Compostela, 15782 Santiago de Compostela, Spain
[d] National Council of Research, Institute of Nanostructured Materials (CNR-ISMN), URT of Messina c/o, Department of Chemical, Biological, Pharmaceutical and Environmental Sciences, University of Messina, Viale F. Stagno D'Alcontres 31, 98166 Messina, Italy
[e] Department of Molecular Medicine, Arabian Gulf University, Manama 329, Bahrain

ARTICLE INFO

Keywords:
3D printing
Anti-biofilm
Thymol
Zinc
Isothermal microcalorimetry
Xanthan gum
Guar gum
Cyclodextrin

ABSTRACT

Biofilm formation on biological and material surfaces represents a heavy health and economic burden for both patient and society. To contrast this phenomenon, medical devices combining antibacterial and pro-wound healing abilities are a promising strategy. In the present work, Xanthan gum/Guar gum (XG/GG)-based scaffolds were tuned with thymol and Zn^{2+} to obtain wound dressings that combine antibacterial and antibiofilm properties and favour the healing process. The tuning process preserved the 3D extrusion-based printability of the XG/GG ink. Scaffolds swelling profile was assessed in PBS pH 7.4, and the resistance to compressive forces was studied using a texturometer. The scaffolds microarchitectures were analyzed by SEM, while ATR-FTIR spotlighted the chemical modifications of the customized materials. Thymol and Zn^{2+} release was analyzed in biologically relevant media, showing a burst release in the first hours. The antibacterial properties were confirmed against *S. aureus*, *P. aeruginosa*, and *S. epidermidis* by isothermal microcalorimetry and biofilm viable cell counting. Incorporation of hydroxypropyl-β-cyclodextrin (HPβCD) improved thymol loading (7- and 14-times higher thymol content) and enhanced the antimicrobial and antioxidant performances of the dressing, while the presence of Zn^{2+} strongly potentiated the antimicrobial activity, showing a potent antibiofilm response in both Gram-positive and Gram-negative strains of clinical concern. The thymol and Zn^{2+} combination led to a reduction of 99.95 %, 99.99 %, and 98.26 %, of biofilm formation against *S. aureus*, *P. aeruginosa*, and *S. epidermidis*, respectively. Furthermore, the scaffolds demonstrated good hemocompatibility, cytocompatibility, tissue integration and pro-angiogenic features in an *in ovo* CAM model.

1. Introduction

The arise of bacterial infections linked to biofilm formation on biological and material surfaces is one of the most urgent topics nowadays. It can lead to severe consequences and long-term patients hospitalization, representing also a heavy burden for the healthcare costs (Depypere et al., 2020; Górecki & Babiak, 2009; Sandiford et al., 2020). Triggering causes of infection can be the bacterial colonization of the implantable material, the intraoperative inoculation of bacteria, or a contamination of the open fracture or wound site. The bacterial colonization of medical devices usually leads to the formation of a biofilm that protects them from the antibiotics action, increasing 100–1000

* Corresponding author at: Department of Drug and Health Science, University of Catania, Viale A. Doria 6, 95125 Catania, Italy.
** Corresponding author at: Departamento de Farmacología, Farmacia y Tecnología Farmacéutica, Faculty of Pharmacy, Universidade de Santiago de Compostela, 15782 Santiago de Compostela, Spain.
E-mail addresses: valeria.pittala@unict.it (V. Pittalà), carmen.alvarez.lorenzo@usc.es (C. Alvarez-Lorenzo).

https://doi.org/10.1016/j.carbpol.2024.123069
Received 6 October 2024; Received in revised form 17 November 2024; Accepted 25 November 2024
Available online 30 November 2024

times the minimum antibiotics concentrations needed for bacterial eradication, causing a higher risk of antibiotic resistance and side effect onset (Kang et al., 2023). Among the main pathogens, *Staphylococcus aureus*, *Staphylococcus epidermidis, Pseudomonas aeruginosa*, and *Escherichia coli*, including Multiple Drug Resistant (MDR) strains, are the major causes of life-threatening infections. These bacteria have been included in the priority list of the world health organization (WHO) also due to their tendency to develop antibiotic resistance in short term (Bouhrour et al., 2024; Chen et al., 2013; Gbejuade et al., 2015; Khatoon et al., 2018; Tacconelli et al., 2018).

The impaired blood flow of infected necrotic tissues prevents systemically administered antibiotics to reach the target site at sufficient concentration to exert antibacterial action, requiring the combination of systemic and local high antibiotics dosage, increasing the risk of side effects (Depypere et al., 2020). Thus, in this scenario, the development of medical devices able to combine antibiofilm and antimicrobial activity with pro-wound healing capacity is a promising strategy for the management and prevention of soft tissues and musculoskeletal infections. However, two premises should be considered: (i) due to the increasing rate of antimicrobial resistance, substances alternative to antibiotics are preferable; and (ii) the use of non-drug GRAS substances that can be considered as ancillary products may make the regulatory approval of the scaffold biomaterial simpler and faster because of its consideration as a medical device and not as a medicine. Thus, non-drugs and widely-approved safe substances providing antibiofilm and antimicrobial activity are preferred. In this context, natural compounds and inorganic ions possessing multi-therapeutical properties can be a wide source to exploit (Frei et al., 2023; Silva et al., 2016).

In clinical practice, cotton, bandages, and gauzes are among the most utilized wound dressings. These cheap devices primarily have a passive role in the healing process, typically acting as protective barriers while absorbing wound exudates (Farani & Shafiee, 2021). However, they fall short in addressing the individualized needs of patients, and a variety of advanced materials like foams, hydrogels, sponges, and films have appeared in recent years with the aim of actively contributing to the wound healing process, serving as true supports for the tissue under restoration (Laurano et al., 2022). The latest trends in the field focus on 3D printing technologies, preferably using carbohydrate polymers as main components (Pita-Vilar et al., 2023; Seijo-Rabina et al., 2024; Yuan et al., 2023). In a recent work, semisolid extruded (SSE) 3D-printed networks composed of xanthan gum (XG), guar gum (GG), and succinic acid (SA) demonstrated to be a green alternative to plastic medical devices, with the added advantages of having a porous structure resembling the natural extracellular matrix, which provides an optimal microenvironment for water, nutrient, and gas exchange, while facilitating tissue integration by displaying angiogenic and anti-collagenase activity (Virzì et al., 2024). Natural carbohydrate polymers, such as XG and GG, offer interesting advantages for wound healing applications, given their high biocompatibility, biodegradability, low price and versatility of chemical properties. XG is a natural polymer produced in the fermentation process by *Xanthomonas* strains. Its chemical structure consists of a linear β-1,4-D-glucopyranose linked, at the C-3 position in each alternating glucose residue, with a side chain composed of an acetylated d-mannose, d-glucuronic acid, and terminal pyruvated mannose (Hassanisaadi et al., 2025). In contrast, GG is a galactomannan extracted from *Cyamopsis* seed species, and its chemical structure consists of a linear β-1,4-d-mannopyranose chain linked with an α-1,6 bond, in each alternating mannose group, with a galactose residue (Zhang et al., 2024). Both polysaccharides exhibit outstanding physicochemical characteristics, allowing the production of pseudoplastic hydrogels and possessing excellent stability at high temperatures and pH. Thanks to their thickening and emulsifying capabilities, both polysaccharides are widely used in the pharmaceutical, food, and cosmetic industries (Manzoor et al., 2022; Tudu & Samanta, 2023).

The aim of the present work was to tune the XG/GG based scaffolds to obtain a safe medical device that can reduce the risk of biofilm development and produce an antimicrobial response, while promoting the wound healing process. The hypothesis of the work was that hydroxypropyl-β-cyclodextrin (HPβCD) can endow the scaffolds with the capability to host essential oil components, while XG can host divalent metal ions (Zn^{2+}), thus providing complementary mechanisms to prevent biofilm formation. Thymol, a monoterpenoid present in *Thymus vulgaris*, is a Generally Recognized as Safe (GRAS) FDA-approved substance with demonstrated antibacterial and antibiofilm activity against Gram-positive bacteria, together with anti-inflammatory and pro-healing properties (Gabbai-Armelin et al., 2022; Michalska-Sionkowska et al., 2017; Nagoor Meeran et al., 2017; Silva et al., 2016). However, its poor water solubility limits its incorporation in a hydrogel-based system. The formation of complexes with HPβCD, another GRAS excipient, can overcome this problem (Garg et al., 2021). In parallel, Zn salts have also shown wide antimicrobial spectra against both Gram-positive and Gram-negative bacteria. $ZnCl_2$ (GRAS substance) can confer antimicrobial properties to coated devices and fabrics (Holt et al., 2018; Noach et al., 2023). Thus, to achieve an optimized scaffold comprising thymol and Zn^{2+}, the following steps were followed: i) HPβCD-Thymol complexes were obtained and extensively characterized by UV–vis and fluorescence spectroscopy, other than size, PDI and zeta potential analysis; ii) HPβCD-Thymol and free-thymol were loaded into an optimized ink consisting of a 12 % *w/v* dispersion in water of XG/GG 50:50 *w/*w containing SA for crosslinking; the self-healing and viscoelastic properties of the formulated inks were analyzed. The inks were then used to print cylindric porous scaffolds, extensively characterized in terms of structural, mechanical and chemical properties, swelling behaviour, release profile, cytocompatibility, hemocompatibility, and antioxidant effect; and finally iii) the produced thymol-embedding scaffold was loaded with Zn^{2+} to obtain the final tuned scaffolds; their antimicrobial activity was then assessed with advanced microcalorimetric techniques and biofilm viable cells counting. The biocompatibility of the scaffolds was tested by means of an hemolysis test and *in vitro* human mesenchymal stem cells (hMSCs) cell viability test. In addition, the angiogenic and tissue integration properties of the XG/GG based scaffolds were verified in an *in ovo* CAM model.

2. Materials and method

2.1. Materials

Guar gum (GG, G4129, MW = 1717.04 kDa, monosaccharides composition: galactose = 37.38 ± 1.54 %, mannose: 62.62 ± 1.54 %; using the method reported by Zhang et al. (2024)), and xanthan gum from *Xanthomonas campestris* (XG, G1235, MW = 2902.44 kDa, 26 % pyruvation and 96 % acetylation, expressed as a percentage of the number of repeating units, using the method reported by Ruijssenaars et al. (1999), Brookfield viscosity 1 % solution 800–1200 mPa·s, monosaccharides composition: glucose = 45.17 ± 2.94 %, mannose = 32.19 ± 1.7 %, glucuronic acid = 22.64 ± 4.62 % (Zhang et al., 2024)) were purchased from Sigma Aldrich® (Merck, Darmstad, Germany). CP/MAS ^{13}C NMR spectra of XG, GG and XG/GG mixture are available in the Supplementary File (Fig. S1).

HPβCD Kleptose® HP oral grade (MS = 0.85, MW = 1480.7 g/mol) was obtained from Roquette® (Lestrem, France). Thymol (>98.5 %), succinic acid (SA, >99 %), zinc chloride ($ZnCl_2$, ≥98 %), calcium chloride ($CaCl_2$, ≥96 %), Certipur® (ICP multi-element standard solution IV), Triton X-100, sodium chloride (NaCl, >99 %) and formaldehyde solution (37 wt% in H_2O) were purchased from Sigma Aldrich® (Merck, Darmstad, Germany). Phosphate buffer saline (PBS), TrypLE®, Dulbecco's Modified Eagle Medium (DMEM), Gibco™ Antibiotic-Antimycotic, FBS and Alamar Blue™ were purchased from ThermoFisher Scientific (Waltham, MA, USA). Human blood anticoagulated with ethylene diamine tetraacetic acid (EDTA) was provided by Centro de Transfusión de Galicia (Santiago de Compostela, Spain) and obtained from anonymized healthy donors, in agreement with the Spanish

legislation (Law 14/2007 on Biomedical Research). Fertilized hen eggs were provided by Coren (San Cibrao das Viñas, Spain). Simulated Wound Fluid (SWF) composed by 8.298 g of NaCl and 0.368 g of $CaCl_2$ *per* liter of double distilled water (DDW) were prepared in the lab. Tryptic soy broth (TSB) was purchased from Oxoid (Hampshire, UK), Bacto™ yeast and Bacto™ tryptone extract were obtained from Becton, Dickinson and Company (Le Pont de Claix, France). *S. aureus* ATCC 25923 and *E. coli* ATCC 15597 were purchased from (ATCC, Manassas, VA, USA), *P. aeruginosa* PAO1, Lausanne sub-line, was donated by M. Camara (University of Nottingham), and *S. epidermidis* CECT 4184 was provided by CECT (Valencia, Spain).

2.2. Cyclodextrin-thymol complex preparation and characterization

2.2.1. HPβCD/thy complex preparation

The HPβCD/Thymol complex (HPβCD/Thy) was prepared at a HPβCD:Thy 1:2 mol ratio. Specifically, 2.03 mmol of HPβCD (3 g) were dissolved in 3 mL of water at R.T. Successively, 4.06 mmol of thymol (609.89 mg) were added to the solution, and let stir for 48 h, at the same temperature. As control, a 3 mL aqueous solution containing 609.89 mg of thymol was prepared and vigorously stirred at the same conditions. After 2 days, the two solutions were diluted to 10 mL and centrifuged at 5000 rpm for 15 min and successively filtered with a 0.45 μm filter, to remove eventual residues of thymol present in the suspension. The HPβCD/Thy supernatant solution was freeze-dried to obtain a white powder of 2.94 g, while the control supernatant was analyzed by means of an UV − vis spectrophotometer (Agilent 8453, Waldbronn, Germany) to evaluate the experimental solubility of thymol.

2.2.2. Thymol loading, entrapment efficiency and recovery yield

The theoretical loading percentage (T.L., %) was calculated using Eq. (1):

$$T.L.(\%) = \frac{W\ Thy\ (1:1ratio)}{W\ HP\beta CD} \times 100 \quad (1)$$

where "*W Thy (1:1 ratio)*" is the amount of thymol needed for a theoretical 1:1 mol ratio complex and "*W HPβCD*" is the total weight of HPβCD used.

The experimental loading percentage (E.L., %) of thymol in the HPβCD/Thy complexes was assessed, in triplicate, by recording the absorbance at 274 nm (UV–vis spectrophotometer Agilent 8453, Waldbronn, Germany) of freeze-dried HPβCD/Thy complexes solutions (250 μg/mL) prepared in DDW and referring to a calibration curve of thymol in DDW. Thus, the thymol loading percentage was calculated using Eq. (2):

$$E.L.(\%) = \frac{W\ Thy\ in\ HP\beta CD/Thy}{W\ HP\beta CD/Thy} \times 100 \quad (2)$$

where, "*W Thy in HPβCD/Thy*" *is* the total amount of thymol present in the complex and "*W HPβCD/Thy*" is the weight of the complex.

The recovery yield percentage was assessed from the ratio of the mass of the freeze-dried HPβCD/Thy complex obtained with respect to the sum of the amounts of HPβCD and thymol added to prepare the complexes, using Eq. (3):

$$Recovery\ yield(\%) = \frac{W\ HP\beta CD/Thy}{W\ HP\beta CD + W\ Thy} \times 100 \quad (3)$$

The entrapment efficiency percentage (E.E., %) was calculated according to Eq. (4):

$$E.E.(\%) = \frac{W\ thy\ in\ HP\beta CD/Thy}{W\ thy(1:1ratio)} \times 100 \quad (4)$$

2.2.3. Size, PDI, and ζ potential analysis of HPβCD/Thy complex

The size, PDI, and ζ potential of the HPβCD/Thy complex (1 mg/mL in DDW) were analyzed by means of a Malvern Zetasizer Pro (Malvern Panalytical, United Kingdom).

2.2.4. UV–vis and fluorescence analysis of HPβCD/Thy complex

HPβCD/Thy and thymol were dissolved in DDW and diluted to achieve the same thymol concentration. A stock solution of HPβCD/Thy (1 mg/mL in DDW) was prepared and further diluted to 300 μg/mL, 100 μg/mL, and 50 μg/mL. UV–vis spectra were recorded using an Agilent 8453 UV–vis spectrophotometer (Waldbronn, Germany) from 190 nm to 800 nm wavelength range and compared to thymol 31.5 μg/mL, 10.5 μg/mL, and 5.25 μg/mL solutions. The fluorescence spectra were acquired using a Varian Cary Eclipse spectrofluorometer (Agilent, USA), using an excitation frequency of 265 nm, and the emission was recorded in the range from 285 nm to 510 nm. Thymol diluted solutions ranged from 10.5 to 2.62 μg/mL.

2.3. Inks composition, preparation and characterization

For the preparation of 1 mL of non-tuned ink (I-NT), 60 mg of XG (6 % w/v), 60 mg of GG (6 % w/v), and 24 mg of SA (2.4 % w/v) were dispersed with 1 mL of DDW and homogenized with a spatula (Table 1). To prepare the free-thymol embedded hydrogel ink (I-Thy), 1 mg (0.01 % w/v) of thymol was solubilized in 1 mL DDW at 50 °C (melting point) in an ultrasonic bath, sonicating for 15 min (Branson 3510 ultrasonic cleaner). Successively, the obtained thymol solution was used to disperse the polysaccharides/succinic acid powder mixture (60 mg XG, 60 mg GG, 60 mg SA). The HPβCD/Thy containing hydrogel inks (I-T7, I-T14, I-T7+, and I-T14+) were prepared adding the HPβCD/Thy complex as powder to the polysaccharides/succinic acid mixture. The amount of succinic acid was 24 mg for I-T7 and I-T14, while it increased to 37.3 mg for I-T7+ and 50.6 mg for I-T14+ to compensate the increase in cross-linkable species (HPβCD). The prepared hydrogel inks were loaded into a syringe and stored at 4 °C until use.

The self-healing properties of the inks were mechanically tested at 20 °C, in triplicate, using a rheometer (Anton Paar, MCR 302, Austria) fitted with a HPTD 200 Peltier hood and a disposable measuring aluminium plate (15 mm in diameter). The gap was fixed at 1 mm. A five step in amplitude sweep mode test was conducted at a constant frequency of 1 Hz, following an already reported procedure (Conceição et al., 2019; Virzì et al., 2024). The five steps consisted of an alternate application of 0.5 % shear strain for 300 s, followed by 100 % shear strain application for 120 s.

2.4. Scaffold production and characterization

2.4.1. Scaffold printing, freeze-drying and crosslinking process

A SSE Regemat® Bio V1 printer (Regemat 3D, Spain) was fitted with a 5 mL syringe equipped with a 0.6 μm nozzle for the scaffolds 3D printing. Regemat 3D designer software was used for the design of the scaffolds, following previously optimized parameters (Virzì et al., 2024). Specifically, the scaffolds dimensions were set at 10 mm diameter, 3 mm height and 0.41 mm layer height. The infill pattern was set as diagonal, an angle of 90° was used for the ink deposition, while the flow speed was set as 7.00 mm/s. The distance between strands was set at 1.20 mm, and no additional perimeters (walls) were used. Petri dishes were used as printing plates. The printed scaffolds were frozen at −80 °C and then freeze-dried using a Lyoquest −85 Telstar® (Telstar, Terrassa, Spain). Then, the scaffolds were placed in a 6 mL glass injection vials (ø 22 mm x h 40 mm), sealed with rubber stopper and aluminium crimp seal, and simultaneously sterilized and crosslinked in a single step process at 121 °C, 1 atm for 20 min, using a RAYPA AES-12 autoclave (RAYPA, Terrassa, Spain).

2.4.2. Structural evaluation

After freeze-drying, scaffolds ($n = 5$) were randomly taken from the produced set, weighed and their structural features were evaluated. A

Table 1
Composition of the inks (1 mL) expressed as total amount and as weight/volume percentage (in parenthesis), and code names of the obtained scaffolds. DDW was used as dispersant.

Ink code	XG in mg (w/v %)	GG in mg (w/v %)	SA in mg (w/v %)	Free-thymol in mg (w/v %)	HPβCD/Thy in mg (w/v %)	Scaffold code
I-NT	60 (6.0 %)	60 (6.0 %)	24 (2.40 %)	–	–	S-NT
I-Thy	60 (6.0 %)	60 (6.0 %)	24 (2.40 %)	1 (0.1 %)	–	S-SA
I-T7	60 (6.0 %)	60 (6.0 %)	24 (2.40 %)	–	66.5 (6.65 %)	S-T7
I-T14	60 (6.0 %)	60 (6.0 %)	24 (2.40 %)	–	133 (13.3 %)	S-T14
I-T7+	60 (6.0 %)	60 (6.0 %)	37.3 (3.73 %)	–	66.5 (6.65 %)	S-T7+
I-T14+	60 (6.0 %)	60 (6.0 %)	50.6 (5.06 %)	–	133 (13.3 %)	S-T14+

precision calliper was used to measure their height and diameter. The scaffolds were visually assessed after printing, freeze-drying, cross-linking, and swelling using an Olympus SZ-CTV stereomicroscope (Olympus, Tokyo, Japan). SEM images of the scaffold S-T7+ were taken before and after swelling in DDW for 30 min and freeze-dried, while the zinc ions loaded scaffolds (S–Zn and S–TZn) were directly analyzed after loading and freeze-drying process. The freeze-dried scaffolds were sputter-coated with gold using a Quorum T50T S plus (Quorum, Laughton, UK) applying a current of 20 mA for 1.5 min and visualized using an EVO LS 15 SEM (Zeiss, Oberkochen, Germany).

2.4.3. Swelling test

Crosslinked scaffolds ($n = 3$) were weighed (*W scaffold dried)* and individually placed in vials containing 5 mL of PBS pH 7.4, kept at 37 °C a and 100 rpm for 7 days. At 2 h, 1, 3, and 7 days the scaffolds were removed from the buffer, rapidly wiped with a piece of paper, and then weighed (*W scaffold wet)*. The swelling percentage was calculated using Eq. (5):

$$Swelling\% = \frac{W\ scaffold\ wet - W\ scaffold\ dried}{W\ scaffold\ dried} \times 100 \quad (5)$$

2.4.4. Texturometer compression analysis

Mechanical properties of the scaffolds were measured, in triplicate, at different swelling time (dry, 30 min and 7 days), using a TA.XTplus Texture Analyzer (Stable Micro Systems, Surrey, UK) fitted with a 5-Kg load cell. The test consisted in applying five consecutive compression/decompression forces of 1 kg, using a crosshead speed of 0.2 mm/s and an activation force of 0.001 kg (Virzì et al., 2024). The force-deformation curves were recorded and plotted, and peak areas (work) were calculated. The Young's modulus values were estimated as the slope of the initial linear region of the force/area *vs.* relative strain plots.

2.4.5. Zn^{2+} loading

Crosslinked scaffolds (S-NT and S-T7+) were immersed in a 10 mM $ZnCl_2$ solution (5 mL) in DDW for 30 min at 100 osc/min. Then, the scaffolds were rapidly rinsed into a falcon tube containing 50 mL of DDW to remove unbound $ZnCl_2$, frozen at −80 °C and freeze-dried. To quantify the amount of Zn^{2+} loaded, S–Zn and S-TZn scaffolds were immersed in 10 mL of SWF for 72 h. Then, the solution was analyzed with a SPECTRO GENESIS Inductively Coupled Plasma - Optical Emission Spectrometry (ICP-OES) (Spectro Ametek, Kleve, Germany) equipment, and the amount of zinc ions extracted from the medium was quantified by means of a calibration curve performed using Certipur® (ICP multi-element standard solution IV, Merck, Darmstad, Germany).

2.4.6. Release studies

The release profile of Thymol and HPβCD/Thy was assessed, in triplicate, by immersion of scaffolds S-Thy, S-T7+, and S-T14+ in 5 mL of PBS pH 7.4. Aliquots (100 μL) of the release medium were withdrawn at prefixed timepoints (30 min, 1, 2, 4, 8 and 24 h), diluted to 1 mL and their absorbances were recorded at 274 nm (Agilent 8453 UV–vis spectrophotometer, Waldbronn, Germany). The released amount was quantified by means of a calibration of curve of thymol in DDW.

The Zn^{2+} release from the scaffolds S–Zn and S-TZn was assessed, in triplicate, using the ICP-OES technique, which was calibrated as explained above. Specifically, the S–Zn and S-TZn scaffolds were immersed in 5 mL of SWF (solvent chosen to simulate Zn^{2+} release in wounds, and whose ions did not interfere with the ICP-OES analysis). Aliquots (100 μL) of the release medium were withdrawn at prefixed timepoints (30 min, 1, 2, 4, 6, 8, 24, and 72 h) and diluted to 3 mL.

2.4.7. ATR-FTIR scaffold analysis

An ATR-FTIR analysis of the scaffolds was conducted using a Gladi-ATR (Pike Technologies, Madison, WI, USA). Before the analysis, S-NT, S-Thy, S-T7+, and S-T14+ scaffolds were previously immersed in 5 mL of DDW for 30 min to remove the excess of SA, and then freeze dried. Conversely, the scaffolds S–Zn and S–TZn were analyzed directly.

2.5. Biocompatibility screening

2.5.1. Hemolysis test

The hemocompatibility of the scaffolds (S-NT, S-Thy, S-T7, S-T14, S-T7+, and S-T14+), Thymol, HPβCD, HPβCD/Thy, and $ZnCl_2$ was carried out according to a protocol explained elsewhere (Farto-Vaamonde et al., 2022). Human volunteers blood (Centro de Transfusión de Galicia, Spain) previously anticoagulated was diluted with a NaCl 0.9 % *w/v* solution, to obtain a 3.5 % *v*/v diluted blood solution. Thymol, HPβCD, HPβCD/Thy, and $ZnCl_2$ were dissolved into an appropriate solvent and added to plastic tubes containing 900 μL of diluted blood to achieve the desired concentration (final volume 1 mL, NaCl 0.9 % w/v was used to fill the remaining volume to 1 mL when required). Thymol was dissolved in DMSO and the final concentrations in the tubes were 2.5, 2.0, 1.5, 1.0, 0.5, and 0.25 mg/mL (maximum DMSO content: 10 % *v*/v). HPβCD and HPβCD/Thy were dissolved in NaCl 0.9 % w/v and the final tested concentrations were 23.75, 19, 14.25, 9.5, 4.75, and 2.37 mg/mL. $ZnCl_2$ was dissolved in NaCl 0.9 % w/v and the final concentrations were 100, 75, 50, 25, 10, and 5 mM. Negative controls were 10 % v/v DMSO in diluted blood and 0.9 % v/v NaCl solution, while the positive control was 4 % v/v Triton-X in DDW. After incubation, for 1 h at 37 °C, 100 rpm, the vials were centrifuged for 10 min, 10,000 rpm at R.T. Scaffolds S-NT, S-Thy, S-T7, S-T14, S-7+ and ST14+ were analyzed after being swelled in 5 mL of PBS pH 7.4 for 30 min. The S–Zn and S–TZn scaffolds were analyzed dried. The scaffolds were individually placed into 15 mL plastic tubes containing 5 mL of diluted blood, and incubated for 1 h at 37 °C, 100 rpm.

After incubation, the scaffolds were removed, and the diluted blood solution remaining in the 15 mL plastic tubes were centrifuged for 10 min, 4500 rpm at R.T.

The supernatants (150 μL) were transferred into a 96 well plate, and the absorbance (Abs) of the hemoglobin present in the supernatants at 540 nm was recorded using a Fluostar Optima, (BMG Labtech, Ortenberg, Germany). Hemolysis percentage was obtained using Eq. (6):

$$Hemolysis\ (\%) = \frac{(AbsS - AbsN)}{(AbsP - AbsN)} \times 100 \quad (6)$$

where "*AbsS*" represents the absorbance derived from scaffolds hemolytic effect, "*AbsN*" is the absorbance of the negative control, while "*AbsP*" is the absorbance of the positive control.

2.5.2. Preliminary in vitro hMSCs cytocompatibility

The hMSCs (bone marrow derived mesenchymal stem cells – normal human, ATCC PCS-500-012) were expanded in α-MEM enriched with 10 % FBS and 1 % antibiotic-antimycotic (complete medium). The culture medium was replaced every other day and cells were split when reaching 70 % confluency. hMSCs were seeded in 48-well plates with a cell density of 40,000 cells/well and let to attach for 24 h. Before testing, the scaffolds were autoclaved at 121 °C, 1 atm for 20 min to allow sterilization and crosslinking. Scaffolds were soaked in 5 mL of PBS pH 7.4 for 30 min (to remove organic acid excess and simulate conditions of Zn^{2+} loading). The scaffolds ($n = 3$, ø 10 mm x h 3 mm) were placed in direct contact with the cell monolayers for 24 h. Then, they were removed, and the media was recovered and used for the antioxidant activity test (Section 2.5.4). Cell viability was quantified using Alamar blue™ reagent. Complete medium supplemented with 10 % of Alamar blue™ reagent was added to each well, and the plate was incubated for 2 h. Then, supernatants (150 µL) were transferred into a 96 well plate, and a plate reader (Fluostar Optima, BMG Labtech, Ortenberg. Germany) was used to measure the emitted fluorescence at 580 nm after excitation at 540 nm.

2.5.3. In vitro "dynamic" cytocompatibility test

hMSCs were seed in a 24-well plate (well area: 1.9 cm^2) in 1.5 mL with a cell density of 34,545 cells/well and let them attach for 24 h. The density was chosen on the basis of preliminary experiments, considering that 40,000 cell/well were used to test scaffolds cytocompatibility in a 48 well plate (well area: 1.1 cm^2) for an entire scaffold (Virzì et al., 2024). Testing half scaffolds in a 24 well plate with a cell density of 34,545 cells/well allowed to maintain the same cell density *per* well area *per* amount of scaffold. Moreover, using 1.5 mL of media, the scaffolds cytocompatibility tests can also simulate the same conditions used for antimicrobial studies (1 scaffold immersed in 3 mL of broth, Section 2.6).

The wound is a dynamic system, in which the production of exudates and continuous cell migration must be taken into account for a more accurate mimicking during *in vitro* testing. A wound infected by *S. aureus* generally produces a median of 2.8 mL/cm^2/24 h, which corresponds to a production of 0.116 µL/cm^2/h of exudate (Dealey et al., 2006). Considering a well of a 24-well plate as the wound area, 200 µL of media content would be replaced every hour (for 8 h) by fresh media containing cells density at 60,000 cells/mL, which corresponds to 12,000 cells *per* 200 µL (mimicking cells migration to the wound area).

After cell attachment, the non-attached cells were removed by discarding the media, and the well was filled with fresh α-MEM (1.5 mL) and half scaffolds ($n = 3$, ø 5 mm x h 3 mm) were put in contact with the cell monolayer for 24 h. Before testing, the scaffolds were autoclaved at 121 °C, 1 atm for 20 min to allow sterilization and crosslinking. A fixed volume of the media (200 µL) was removed every hour and replaced with new media (200 µL) containing hMSCs, until replacing it all (after 8 h). During time 0, three wells were used to calculate the initial cell viability (I.C·V.), which ideally can mimic the number of viable cells that the wound possesses before being in contact with the scaffolds. The I.C.V. was measured with Alamar blue, incubating the cells for 2 h with Alamar blue reagent (diluted 1:11 in α-MEM), and transferring 150 µL of incubated solution in 96 well plates. Then, the emitted fluorescence was recorded at 580 nm after excitation at 540 nm with a plate reader (Fluostar Optima, BMG Labtech, Ortenberg. Germany). After 24 h incubation, the scaffolds were removed, and the cell viability was measured by Alamar blue as previously described in Section 2.5.2.

2.5.4. Scaffolds antioxidant activity

The culture media recovered during the static *in vitro* hMSCs cell viability was used to check the scaffold's antioxidant activity (AA). The AA was determined using ABTS (2,2′-azino-bis-(3-ethylbenzothiazoline-6-sulfonic acid) reagent, following an already known methodology (Castillo et al., 2023; Ozgen et al., 2006). In a 96 well plate, 100 µL of serially diluted media was mixed with 100 µL of ABTS reagent (prepared in methanol). The media of hMSCs cultured without scaffolds was used as control. The plate was gently shaken for 10 s and then kept in the dark for 10 min. Successively, the samples absorbance was measured at 730 nm by using a Fluostar Optima microplate reader (BMG Labtech, Ortenberg, Germany). For AA quantification, a calibration curve prepared in Trolox was employed. The AA was expressed as equivalent Trolox millimoles per liter of medium (mmol TRE/L), and the results were the mean of an experiment conducted in triplicate ($n = 3$). The mean anti-oxidant inhibitory concentration (IC_{50}) of the samples was also calculated, and since the concentration of the sample is unknown, it was represented as the dilution factor able to inhibit the 50 % of the ABTS radicals. For this purpose, the recovered media's dilutions were carried out in a range of inhibition between 20 % and 80 % of $ABTS^+$. The following Eq. (7) was used to calculate the dilution able to inhibit the 50 % of the ABTS radicals:

$$Y = aX + b \tag{7}$$

where "*Y*" is the percentage inhibition of ABTS+, "*X*" is the dilution factor, "*a*" and "*b*" are the fitted parameters of the regression line.

2.5.5. In ovo angiogenesis and tissue integration

The tissue integration and angiogenesis capacity of the scaffolds was tested by means of an *in ovo* chorioallantoic membrane (CAM) as described previously (Farto-Vaamonde et al., 2022; Virzì et al., 2024). Fertilized hen eggs (Coren, San Cibrao das Viñas, Spain) were put into an incubator at 37 ± 1 °C and 60 % RH in horizontal position, and periodically rotated to avoid membrane adhesion to the eggshell. On day 3, 3 mL of albumin was removed from the acute pole of the eggs, and a window of ~1 cm × 1 cm was opened on the eggs' side, allowing to check the embryo status. Then, the window was covered with a piece of film to prevent contamination and drying out, and the eggs were put back in the incubator. The eggs manipulation was conducted in sterile conditions.

Before testing, the scaffolds were autoclaved at 121 °C, 1 atm for 20 min to allow sterilization and crosslinking. In addition, the scaffolds S-T7+ were previously soaked into a PBS pH 7.4 solution, to remove the excess of the SA and to simulate the amount of thymol present in the scaffold after Zn^{2+} loading. On the other hand, given that Zn^{2+} supply has been reported to be toxic for the embryos during *in ovo* testing (Sun et al., 2018), the tissue integration and angiogenesis capacity of the scaffolds S–Zn and S–TZn was performed after soaking them into 5 mL of SWF to allow the release of Zn^{2+} in excess. Thus, on day 8, the treated scaffolds ($n = 3$) were individually placed on the CAM. The window was re-covered with new parafilm, and the eggs were returned to the incubator until day 12. On day 12, the window was further enlarged to perform a macro-histological evaluation of the CAM status. Based on the angiogenetic effect and integration of the scaffolds to CAM, a score of integration (SI) was assigned to each scaffold, ranging from 0 (poor integration) to 3 (excellent integration) (Ponce & Kleinmann, 2003). Then, the CAM was fixed with 4 % *v*/v formaldehyde solution for 4 h, and a scaffold-centred circular section of CAM was resected using a surgical blade. The resected CAMs were then transferred into 6 well plates and washed 3 times with PBS pH 7.4, allowing also membrane spreading over the well plate. Images of the resected membranes were taken using an Olympus SZ-CTV stereomicroscope (Olympus, Japan).

2.6. Antibacterial and antibiofilm tests

The antimicrobial and antibiofilm properties of the scaffolds were evaluated against *S. aureus* ATCC 25923, *P. aeruginosa* PAO1, and *S. epidermidis* CECT 4184, using isothermal microcalorimetry complemented by colony forming units (CFUs) counting to evaluate the formation of the biofilm over the scaffolds. *S. aureus* and *S. epidermidis* were cultured in 1 % NaCl Tryptic Soy Broth (TSB-1), while *P. aeruginosa*

was cultured in Luria-Bertani's Lysogenic Broth (LB) (10 g/L tryptone; 5 g/L yeast extract, 10 g/L NaCl). Both culture media were prepared in distilled water and autoclaved before use (121 °C, 1 atm, 20 min). All the scaffolds were sterilized at the same conditions.

2.6.1. Isothermal microcalorimetry

An I-Cal Flex Isothermal calorimeter system (Calmetrix, Needham, MA, USA) equipped with 8 cells (20 mL capacity) was used to register the metabolic heat of bacteria. The equipment was previously stabilized and calibrated at 37 °C before starting the analysis.

To obtain the inoculum, the bacteria were seed on TSA plate and cultured for 24 h at 37 °C. Subsequently, a single bacterial colony was taken from the agar plate with a swab and transferred into 10 mL of broth to form a pre-inoculum, which was cultured for 24 h at 37 °C. Then, 1 mL of pre-inoculum was put into a 1.5 mL tube (in duplicate) and centrifuged at 13,000 rpm for 3 min. The supernatant was removed, and the pellet was resuspended with fresh broth. The Optical Density (O.D.) of the solution was read at 600 nm with an UV–vis spectrophotometer (Helios Omega, Thermofisher, MA, USA), and was used to obtain an inoculum of 50 mL with an appropriate O.D.; O.D. of *S. aureus* and *S. epidermidis* were adjusted to 0.1, while *P. aeruginosa* was adjusted to 0.01. Then, 3 mL of bacteria inoculum was used to fill the calorimeter tubes, and one scaffold was placed in each tube; tubes containing only the bacteria inoculum were used as control (Farto-Vaamonde et al., 2022).

Changes in energy as a function of time were recorded as power (mW) during 72 h for *S. aureus* and *S. epidermidis* or 24 h for *P. aeruginosa*. Data were collected every 10 s for the first hour and every 1 min for the successive hours, using the I-Cal Logger software. In all experiments, two calorimeter cells were reserved and used for the monitoring of bacteria growth in culture media without scaffolds, while the other calorimeters cells were used to measure the metabolic heat of bacteria in contact with the scaffolds. All experiments were carried out in duplicate, and the data were analyzed using I-Cal Reports software and plotted using GrapPad Prism.

2.6.2. Biofilm formation quantification

After incubation in the microcalorimeter, the biofilm formed on the scaffolds was evaluated by the determination of colony-forming units (CFUs) following previously reported protocols (Farto-Vaamonde et al., 2022; Vivero-Lopez et al., 2021). The scaffolds were withdrawn from the bacteria inoculum, placed into 24-well plates, and washed three times by soaking them into 2 mL of sterile PBS pH 7.4 for 5 min to remove planktonic bacteria. Then, each scaffold was placed in a sterile tube containing 2 mL of sterile PBS pH 7.4, sonicated in a sonicator bath (Branson CPX8800 Ultrasonic Cleaner, 40 kHz) for 15 min, and then vortexed for 30 s. The suspensions of detached bacteria in PBS solution (0.5 mL) were serially 1:10 diluted with 4.5 mL of culture broth (TSB for *S. aureus and S. epidermidis*, while LB for *P. aeruginosa*). Afterwards, 100 μL of the diluted suspensions were seeded on TSA-1 (for Gram-positive) or LB petri dishes (for Gram-negative), using a Digralsky spreader until the liquid was completely absorbed by the agar, in triplicate. Then, the agar plates were incubated at 37 °C for 24 h, protected from light. After incubation, bacteria colonies were counted, and the number of CFUs/scaffold was calculated considering the dilution factor (df) and the total detachment volume (tdv) using Eq. (8):

$$\frac{CFUs}{scaffold} = \frac{No.colonies \times df \times tdv\left(\frac{mL}{scaffold}\right)}{volume\ inoculated\ on\ culture\ plate(mL)} \quad (8)$$

2.7. Statistical analysis

The statistical analysis was carried out by means of GraphPad Prism (GraphPad software, La Jolla, CA, USA) software, using unpaired *t*-test with Welch's correction, Kruskal-Wallis non-parametric test, and one-way Analysis of Variance (ANOVA) and Tukey's multiple comparison post-tests (with Brown Forsythe test, and Shapiro-Willis test). Significant differences were considered for $p < 0.05$. 0.1234 (ns), 0.0332 (*), 0.0021 (**), 0.0002 (***), <0.0001 (****).

3. Results and discussion

3.1. Components selection

Low-cost, biocompatible, biodegradable, and steam-heat sterilizable SSE-3D-printed medical devices capable of preventing infections in wounds were developed using the natural polysaccharides XG and GG. A schematic diagram illustration the chemical structures of XG and GG and how they blend to form a 3D-printing gel or bioink is depicted in Fig. 1. Starting from a previous optimization (Virzì et al., 2024) and as a step-forward, the present work was focused on tailoring XG/GG 3D-printed based scaffolds to confer them antibiofilm and antibacterial properties and to reinforce the wound healing properties. Seeking alternatives to common antibiotics is a priority nowadays to contrast the rising antibiotic resistance. For that purpose, the XG/GG scaffolds were loaded with the natural compound thymol and the cationic ion Zn^{2+}, separately or in combination. The antibacterial activity of thymol is related to its ability to cause membrane lipid layer destabilization and oxidation, and consecutive membrane depolarization and damage, that can lead to leakage of intracellular component and cell death (Li et al., 2022; Tian et al., 2021). Moreover, it can disrupt the Quorum Sensing (QS) mechanism of several Gram-positive bacteria, including multi drug resistant *S. aureus* (Kowalczyk et al., 2020; Nostro et al., 2007; Silva et al., 2016). In addition, thymol has anti-inflammatory and wound healing activities, promoting angiogenesis, improving fibroblasts growth, and helping bone regeneration *in vitro* and *in vivo* (Costa et al., 2019; Gabbai-Armelin et al., 2022; Lavanya et al., 2023; Sapkota et al., 2018). Nevertheless, despite its promising biological activities, the low solubility of thymol in water (0.98 μg/mL) hinders its loading within a hydrogel ink. The inclusion of high amounts of non-soluble thymol crystals into SSE-3D-printing inks could lead to the nozzle clogging, interfering with the printing process and causing a non-homogenous distribution within the network. Thus, HPβCD was used to increase thymol solubility by forming an inclusion complex (Celebioglu et al., 2018; Garg et al., 2021).

Regarding Zn^{2+} ions loading, the carboxylic groups present in the XG molecular structure can coordinate divalent ions (Virzì et al., 2024), favouring the uptake into the scaffolds and modulating their release. Zinc ions possess promising antimicrobial and antibiofilm properties, other than a broad spectrum of action. Indeed, $ZnCl_2$ coated intranasal silicone splints have shown antibiofilm properties against both *S. aureus* and *P. aeruginosa*, even after prolonged bacteria exposure for 168 h (Noach et al., 2023). Moreover, fabrics immersed in $ZnCl_2$ solution exhibited long-lasting antimicrobial efficacy on a variety of pathogens, showing low toxicity in human cells (Holt et al., 2018). Water solubility of $ZnCl_2$ may allow an easy incorporation into the XG/GG ink, but Zn^{2+} loading was performed after the scaffolds production and crosslinking process to avoid premature release when the scaffolds had to be soaked in PBS or DDW to remove the excess of the crosslinker (SA). Thus, the loading of Zn^{2+} was performed simultaneously to the washing procedure in a single step, by soaking the scaffolds into a $ZnCl_2$ aqueous solution. Furthermore, charging the scaffolds with Zn^{2+} after the production process allowed to first obtain, fully characterize, and optimize the scaffolds containing thymol, and subsequently, load them also with Zn^{2+}. This approach enabled building the final desired scaffold "brick after brick", adding new features during the production process stepwise and optimizing after each step.

3.2. HPβCD/Thy complex preparation and characterization

The first step of the thymol-containing scaffolds production was the preparation and characterization of HPβCD/Thy complexes (Table 2). A

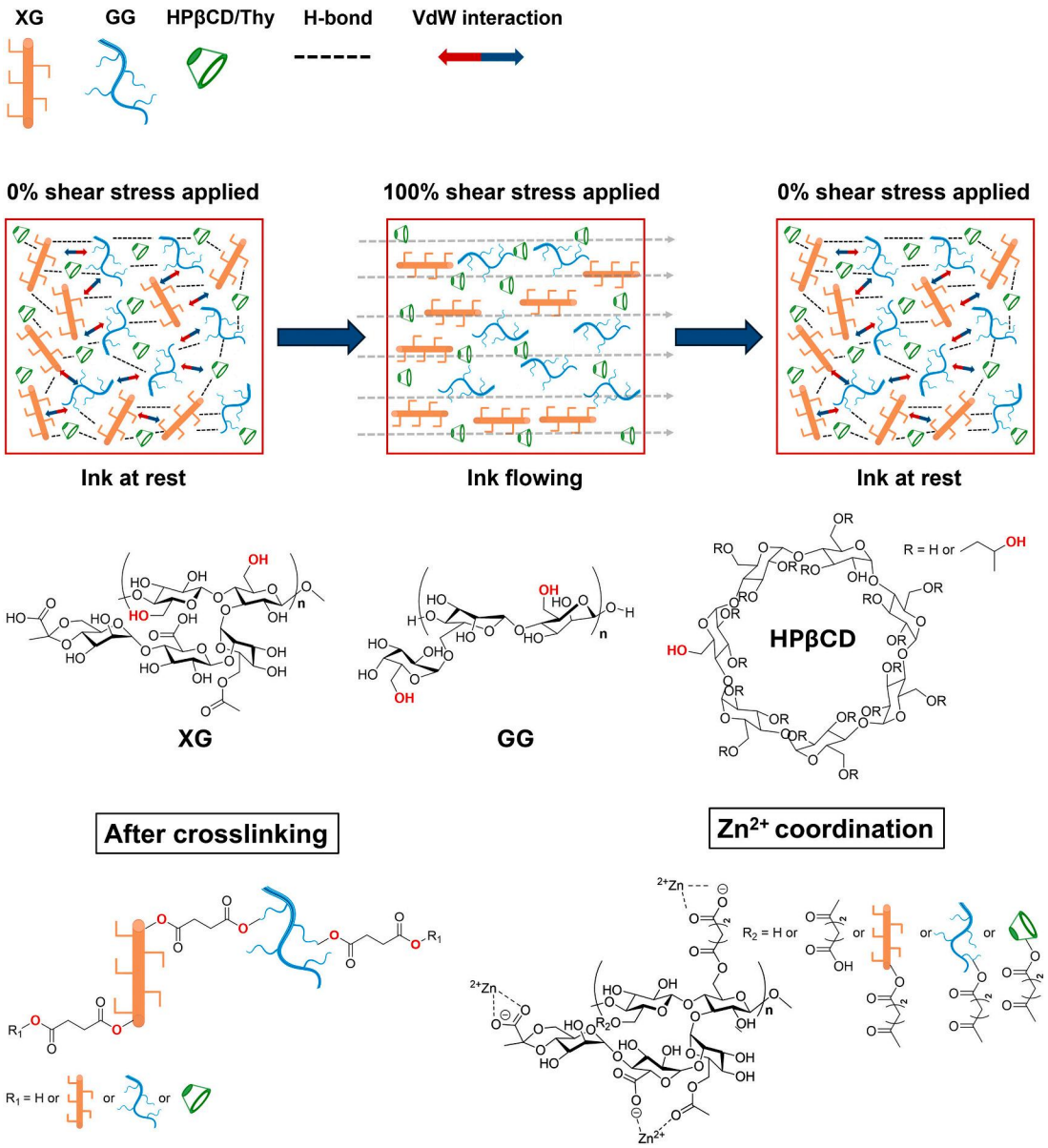

Fig. 1. Schematic illustration of the tuned XG/GG ink rheological behaviour, crosslinked scaffold structure, and Zn^{2+} coordination mechanism. Before cross-linking, hydrogen bonding and van der Waals interactions between XG, GG, and succinic acid dictate the behaviour of the inks. The most reactive and less sterically hindered -OH groups (primary -OH, which have the highest probability to take part to crosslinking reaction) in XG, GG and HPβCD are depicted in red. During the cross-linking succinic acid forms covalent bonds with XG, GG, and HPβCD. Once the scaffold is formed, Zn^{2+} can be immobilized through coordination with XG carboxylic acid groups.

Table 2
Theoretical thymol loading (T.L.), experimental loading (D.L.), recovery, and entrapment efficiency (E.E.) values, $n = 3$.

Complex	T.L. (%)	D.L. (%)	Recovery (%)	E.E. (%)
HPβCD/Thy	10.1	10.5 ± 0.04	81.4 ± 3.8	103.7 ± 0.4

molar ratio of HPβCD:Thy 1:2 was used to saturate the cyclodextrin cavities. Thymol solubility in water was experimentally determined to be 0.9 mg/mL. Thus, considering a final volume of 10 mL of DDW after centrifugation, 9 mg of free-thymol are expected to be in the final formulation. Indeed, the experimental thymol loading was slightly higher than the theoretical one, calculated with a HPβCD:Thy 1:1 ratio, because of the slight solubility of thymol in DDW. Nevertheless, as expected, the excess allowed the complete saturation of the cyclodextrin cavities, maximizing the entrapment efficiency (E.E. =103.7 ± 0.4 %). Indeed, the 3.7 ± 0.4 % of excess can matches with the 9 mg of thymol solubilized by DDW. The recovery of the HPβCD/Thy complex was of 81.4 %.

The absorption spectra of HPβCD/Thy in DDW were matched with those of free thymol at the same thymol concentrations, with a peak at 274 nm (Fig. S2A). HPβCD/Thy complexes diluted to 250 μg/mL were dissociated, allowing precise thymol quantification. The complex was characterized for its size, PDI, and ζ potential, showing an homogenous nanoaggregate population with a size of 116.1 ± 2.74 nm, a PDI of 0.117, without larger aggregates or floccules. A ζ potential of −10.98 mV was obtained (Fig. S2B). The fluorescence profiles of the HPβCD/Thy and thymol solutions also showed peaks of similar intensity, but slightly red shifted (~4 nm), accordingly with previously reported data in literature (Sun et al., 2021). As control, a 300 μg/mL of pristine HPβCD solution was also analyzed, and no fluorescence emission was recorded in all the examined emission ranges (Fig. S2C).

3.3. Inks preparation and rheological properties

Free-thymol and HPβCD/Thy were incorporated into the XG/GG based inks (composition in Table 1) and their effects on the ink properties were compared. To prepare the free-thymol containing ink (I-Thy), a concentration of 1 mg/mL in DDW was chosen based on the maximum solubility of thymol in water, given that non-solubilized thymol crystals can clog the 3D-printer nozzle. The thymol suspension was sonicated at 50 °C to reach thymol melting point (m.p. 49–51 °C), and thanks to ultrasound and heat it was possible to obtain a clear solution, which was essential to produce a well homogenized ink. On the other hand, the freeze-dried HPβCD/Thy complex was mixed directly as a powder with the polysaccharides and crosslinker, and the powder mixture was successively dispersed with DDW. The use of this procedure did not only speed-up the preparation, but also allowed to prepare a "ready-to-mix" powder blend to be dispersed on demand. Furthermore, the ink can be loaded with a higher dose of HPβCD/Thy than if the free natural compound were used. Indeed, the HPβCD/Thy complex allowed increasing 7-fold (I-T7 and I-T7+) and 14-fold (I-T14 and I-T14+) the concentration of thymol compared to I-Thy. A different amount of crosslinker was used for I-T7+ and I-T14+ (20 % of the XG/GG+ HPβCD/Thy complex weight) compared to I-NT, I-Thy, I-T7 and I-T14 (20 % of the XG/GG weight) to take into account the participation of the HPβCD/Thy complex in the crosslinking process.

After formulation, the self-healing properties of the produced inks were evaluated in a test consisting of five steps in amplitude sweep. As already reported, a 12 % XG/GG blend (50:50 w/w) possessed optimal rheological profile for SSE 3D-printed, even when the organic acid crosslinker was added, generating scaffolds with an adequate resolution and shape-fidelity (Virzì et al., 2024). Here, the effect of thymol addition in the free form or as HPβCD/Thy complex was evaluated (Fig. 2). All tested inks showed viscoelastic solid behaviour (G' > G") at 0.5 % of shear stress, while they behaved as a viscoelastic fluid (G" > G') at 100 % shear stress. Moreover, the inks evidenced an appropriate self-healing behaviour when the applied shear stress decreased from 100 % to 0.5 %, recovering the initial G' values.

The rheological behaviour observed in the XG/GG blend can be attributed to the different molecular flexibility of the two polysaccharides. GG has a flexible structure, while XG has a rigid, rod-like conformation (Schreiber et al., 2020). This contrast allows each polysaccharide to behave independently, creating an ink in which chemical interactions (*e.g.*, hydrogen bonds, van der Waals interactions) easily break down under shear stress, but rapidly reform its structure and interactions when the stress is removed, allowing the 3D-printed shape to be maintained (Fig. 1). The addition of thymol, HPβCD/Thy, or higher amounts of cross-linker did not compromise the self-healing properties of the original ink, which seemed to depend solely on the behaviour of XG and GG, at the concentrations tested.

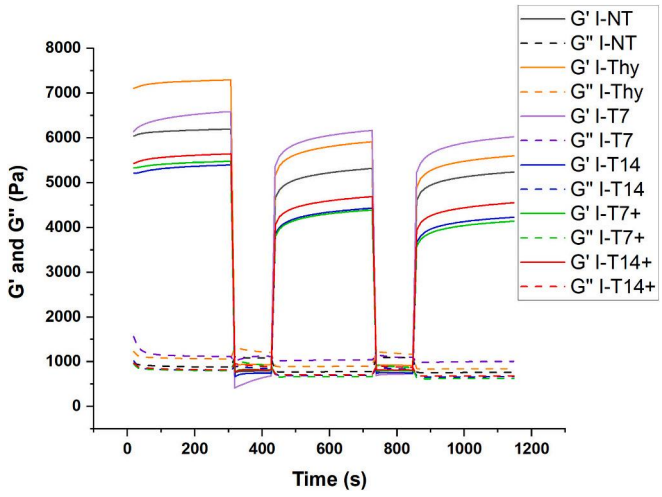

Fig. 2. Storage (G') and loss (G") moduli of the inks recorded at 20 °C.

3.4. Scaffold production and characterization

3.4.1. Scaffold production

The inks were used for printing cylindric scaffolds (ø 10 mm x h 3 mm) directly on Petri dishes to facilitate freezing, freeze-drying, and storage. All inks proved to be suitable for producing scaffolds with the required features, without generating clog of the nozzles or problems during printing (Fig. 3). Right after printing, the scaffolds were frozen at −80 °C and then freeze-dried. The freeze-dried scaffolds did not collapse during the procedure, maintaining the original shape with high fidelity (Table S1). Also, the weight of the scaffolds showed intra-group homogeneity (Table S1). Then, the freeze-dried scaffolds were crosslinked by a steam-heat catalyzed reaction in autoclave at 121 °C, 1 atm for 20 min. It was already demonstrated that in presence of heat, the reaction of succinic acid with OH groups of the pyranose chains of gums generates an intricate network of hydrophobic ester bonds, modifying the swelling, mechanical properties, and hydrophobicity of the scaffolds (Thessrimuang & Prachayawarakorn, 2019). After the process, the scaffolds colour changed to a yellowish colour (Fig. 3). Interestingly, S-NT, S-Thy, S-T7+, and S-T14+ showed a more marked yellowish colour, while S-T7 and S-T14 maintained a more whitish colour (Fig. 3). Thus, higher succinic acid amount led to darker colour (S-T7 *vs* S-T7+, and S-T14 *vs* S-T14+), which may reflect higher crosslinking degree.

3.4.2. Swelling test

A controlled swelling behaviour of an implantable biomaterial is an important feature to be considered for design and application. Indeed, the rapid swelling of a scaffold can nullify the work done during the 3D-printing process to confer a precise shape, highly reducing the chance of a proper tissue-integration. The PBS buffer pH 7.4 was chosen to mimic the wounds saline exudate (Duan et al., 2020). It should be noted that the pH of damaged skin is highly variable and unlike the typical acidic values of healthy epidermis, pH values close to or even higher than 7 are commonly found in acute wounds during the granulation phase, infected dermis and chronic wounds (Kuo et al., 2020).

All scaffolds (S-NT, S-Thy, S-T7, ST7+, S-T14, and S-T14+) maintained the shape and structural features, even after 7 days immersed in the buffer. However, the amount of liquid absorbed by the scaffolds was somehow different (Fig. 4). After 2 h, no significant difference was seen in the PBS content among S-NT, S-Thy, S-T7, and S-T14, while a lower swelling was recorded for S-T7+ and S-T14+. The same trend was seen after 168 h, when both S-T7+ and S-T14+ swelled far less than S-NT. The presence of HPβCD/Thy did not modify the swelling behaviour of the scaffolds (S-NT *vs* S-T7 and S-T14), while lower amount of PBS was absorbed by the scaffolds prepared with higher amount of succinic acid (S-NT *vs* S-T7+ and S-T14+), confirming higher crosslinking degree. These findings are in agreement with the literature, where polysaccharide-based materials showed higher reticulation rate when the amount of organic acid is increased (Coma et al., 2003). For example, 3D-printed cellulose nanocomposites scaffolds were reported to reduce the swelling as the used amount of citric acid increased (Stiglic et al., 2022). In addition, the crosslinking reaction consumes the hydrophilic functional groups of the polysaccharides (-COOH and -OH), attenuating the hydrophilic interactions with water.

3.4.3. Texturometer compression test

To understand how the presence of HPβCD/Thy and different crosslinker ratio can influence the mechanical properties of the scaffolds, the resistance to compressive forces was evaluated. No significant differences were seen among the dried scaffolds during compression, which proved to resist well to the applied forces (Fig. 5). After 30 min soaking in PBS pH 7.4 buffer, the scaffolds showed differences in

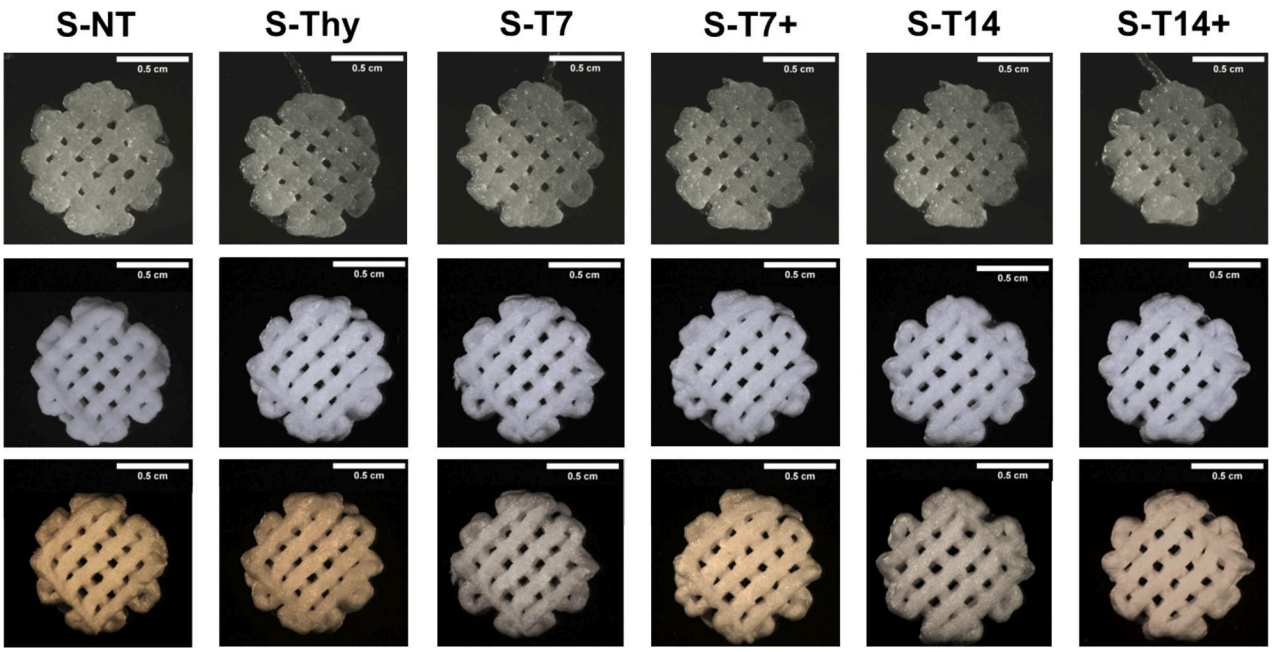

Fig. 3. Scaffolds top view after 3D printing (first row), freeze-drying (second row), and crosslinking/sterilization process (third row).

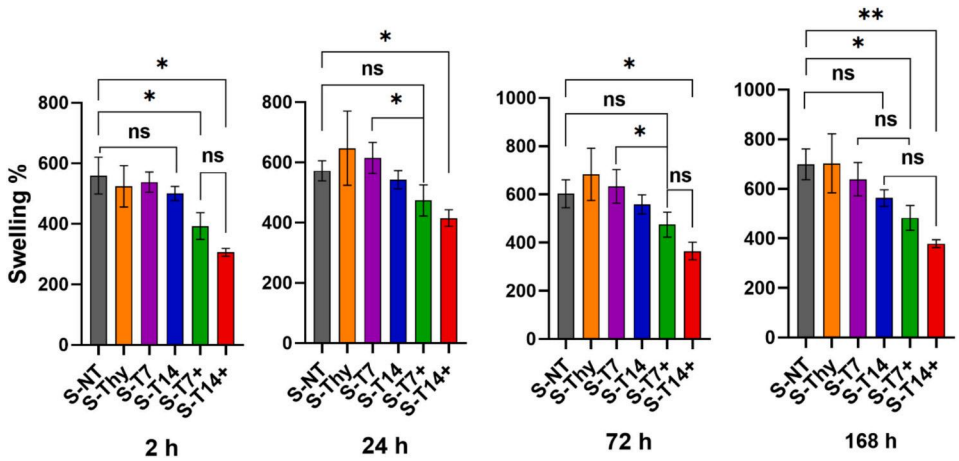

Fig. 4. Scaffold swelling percentage after immersion in PBS pH 7.4. Kruskal-Wallis non-parametric test: $p < 0.05$; 0.1234 (ns), 0.0332 (*), 0.0021 (**), 0.0002 (***), <0.0001 (****), $n = 3$.

resistance to compression (Fig. S3). Indeed, only S-NT, S-Thy, and S-T7+ scaffolds were able to resist five consecutive compressions evidencing pseudo-elastic behaviour, while S-T7, S-T14, and S-T14+ structures were dismantled during the test (Fig. S3 and Fig. 5). The factor conditioning this behaviour is the high amount of HPβCD/Thy, which may compete with the hydroxyl groups of the two polysaccharides for the interaction with succinic acid, leading to a lower crosslinking degree. A higher amount of crosslinker conferred higher resistance to scaffold S-T7+ to the applied forces when compared to S-T7. Conversely, when the HPβCD/Thy content increased more (S-T14+), even a proportional increase in the amount of crosslinker was not enough to maintain toughness and resistance (S-T7+ *vs* S-T14+). Thus, the data revealed that the mechanical properties of the scaffolds are influenced by the HPβCD/Thy and crosslinker content. Indeed, scaffolds S-T7+ showed a good balance between HPβCD/Thy complex and crosslinker content, while the same effect was not seen for S-T14+. Similar findings were previously observed when high proportions of β-cyclodextrin hindered the crosslinking reaction between citric acid and carboxymethylcellulose (CMC) chains. Indeed, other than causing higher sterical hindrance between the polymer chains, disadvantaging the reaction, cyclodextrins can compete for the crosslinking reaction producing the graft of the cyclodextrin to the polymer (Ghorpade et al., 2017).

The free thymol did not negatively influence the scaffolds mechanical properties, but the amount was really low compared to that in the scaffolds prepared with HPβCD/Thy complexes. After 7 days, S-NT, S-Thy, and S-T7+ did not show different mechanical properties when compared to those recorded after 30 min of swelling, showing promising resistance to compression even when exposed to buffer for 7 days. The unique interactions between XG and GG (depicted in Fig. 1) could also explain the "spongy" behaviour of the scaffolds. Indeed, when a balanced cross-linking rate is reached (*e.g.*, in S-NT, S-Thy, and S-T7+), also the final cross-linked scaffolds can benefit from weakly interacting but compatible polysaccharide chains, allowing to obtain a solid structure that can dynamically respond and adapt to compressive stress changes without fracturing, and then pseudoelastically recover the original shape.

Given the appropriate mechanical properties, further experiments were continued only on S-Thy and S-T7+, including the other scaffolds

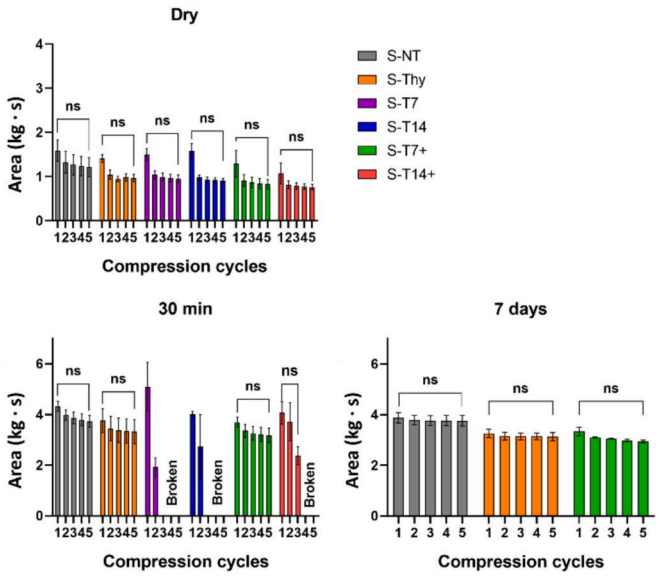

Fig. 5. Area under the curve (work) values after five consecutive compressions cycles for dry scaffolds, and swelled scaffolds in DDW for 30 min and 7 days. Kruskal-Wallis non-parametric test: $p < 0.05$; 0.1234 (ns), 0.0332 (*), 0.0021 (**), 0.0002 (***), <0.0001 (****), $n = 3$.

in some tests to have additional data regarding the effect of higher amount of thymol.

3.4.4. *Thymol release study*

All scaffolds S-Thy, S-T7+, and S-T14+ showed an initial burst release of thymol (Fig. 6). Specifically, thymol released by S-Thy was 70.68 ± 16.13 % just after 30 min, releasing all thymol content after 4 h. Similar fast release was reported in literature for thymol loaded composites. Indeed, thymol-loaded chitosan hydrogels released ~45 % of thymol content after 4 h of study (Alvarez Echazú et al., 2017). Analogous findings were reported for thymol-loaded chitosan-gelatin films and alginate microparticles, releasing most of the thymol content after 24 h (Ahmady et al., 2022). It should be noted that in our case the release tests were carried out by soaking in 5 mL of medium (SWF or PBS pH 7.4) and not using Franz cells to better mimic the situation in which the scaffold is completely exposed to the wound exudates (Ahmad, 2023).

S-T7+ and S-T14+ scaffolds released approximately 50 % of thymol content in the first 30 min, while the remaining thymol content was released with a slower rate, reaching the maximum after 24 h. HPβCD/Thy complexes were previously reported to disassemble very fast, but the release could be attenuated when incorporated into chitosan/polycaprolactone nanofibrous films due to reduced wettability and solvent access (Shen et al., 2022). Our data suggest that the initial burst release can be attributable to the HPβCD/Thy content nearby the scaffold surface, which is followed by the release of the remaining content in the bulk of the scaffold.

The 2-fold content of HPβCD/Thy complex in S-T14+ did not change the release pattern when compared to S-T7+. Considering that Zn^{2+} ions loading was planned to be performed by soaking the scaffolds for 30 min in a $ZnCl_2$ solution, the ability of S-T7+ scaffold to retain approximately 50 % of thymol after 30 min soaking make it suitable for the purpose.

3.4.5. *In vitro biocompatibility and antioxidant tests*

Once ascertained that the release profile can match with the further Zn^{2+} loading, the following tests were performed to evaluate the S-T7+ *in vitro* hemocompatibility, cytocompatibility, and antioxidant effect. Before testing, the scaffolds were immersed in PBS pH 7.4 for 30 min to simulate the behaviour after Zn^{2+} loading.

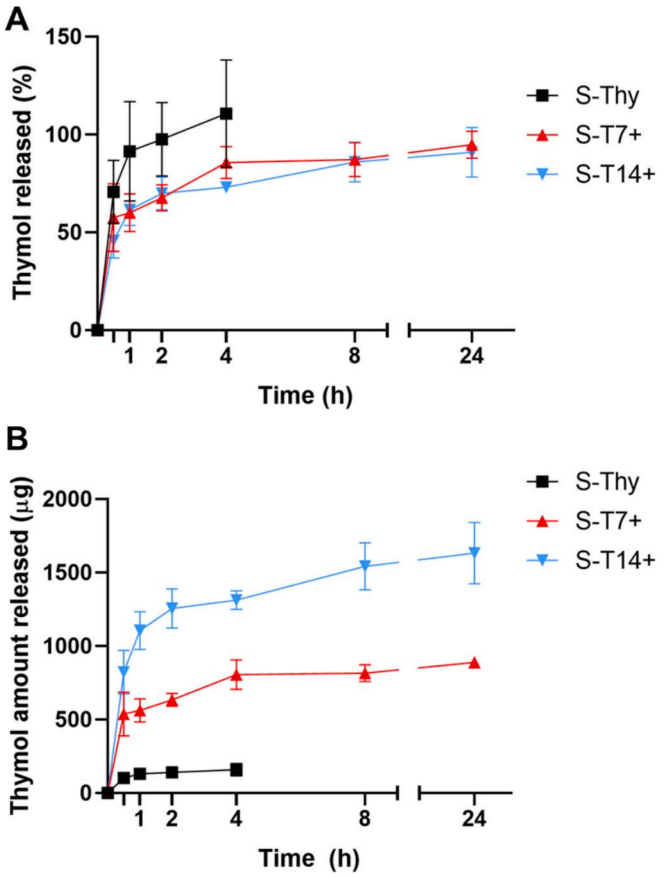

Fig. 6. Thymol release profile expressed in (A) percentage and (B) total amount from scaffolds S-Thy, S-T7+, and S-T14+ in PBS pH 7.4 at 37 °C, 100 osc/min, n = 3.

Regarding hemocompatibility, also free thymol and HPβCD/Thy complex was tested to highlight the effect of the single components (Fig. S4). The results evidenced that thymol possesses a potent hemolytic effect at all tested concentrations, and that the effect is mitigated when forming a complex with HPβCD (Fig. S4). Concentration-dependent effects of thymol have previously been reported, showing a protective effect on erythrocytes at 0.06–1 mM during hypotonic hemolysis, whereas causing lytic effects on erythrocytes at 2–4 mM (Manabe et al., 1987). Similar hemolytic effect has been reported for carvacrol, the isomer of thymol, due to the membrane lipid affinity to the essential oils or to hypotonic effect (Farto-Vaamonde et al., 2022). In addition, literature data confirms the ability of cyclodextrin to mitigate the hemolytic effect of several substances (Hollow & Johnstone, 2022).

Interestingly, the scaffolds S-Thy and S-T7+ showed low or no hemolytic effect, while the scaffold S-T14+ triggered a potent hemolysis (Fig. 7A). Thus, the inclusion of thymol into HPβCD combined with a slower release attenuated the thymol hemolytic effect (*e.g.*, S-T7+). However, when thymol concentration is too high (such as in S-T14+) the hemolytic effect cannot be counteracted.

The scaffolds cytocompatibility was assessed by direct contact with hMSCs monolayers for 24 h. hMSCs were chosen as cell line given their fundamental activity in tissue regeneration and immunomodulation. No toxic effect on hMSCs was caused by the scaffolds, showing high cytocompatibility, comparable to the non-tuned scaffolds (Fig. 7B).

The ability of the scaffolds to produce an antioxidant effect was also evaluated by testing the radical scavenging properties of the culture media eluents (Fig. 7C and D). The results evidenced that S-T7+ had a significantly higher antioxidant activity than S-Thy, which confirmed the advantage of using the HPβCD/Thy complex for scaffolds

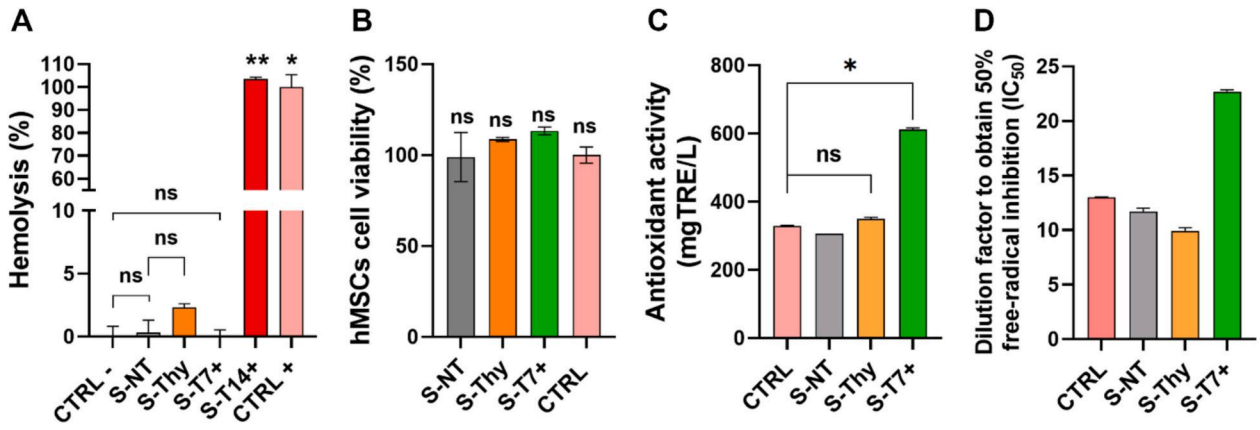

Fig. 7. A) Hemolytic effect of scaffolds S-NT, S-Thy, S-T7+, and S-T14+, CTRL – was NaCl 0.9 % *w/v*, CTRL + was Triton-X 4 % *v/*v; B) hMSCs viability after 24 h contact with scaffolds; C) Antioxidant activity of the culture media put in contact with the scaffolds and hMSCs (CTRL); D) Dilution factor to obtain a 50 % of free-radical inhibition (IC_{50}) of the culture media put in contact with the scaffolds and hMSCs (CTRL). Kruskal-Wallis non-parametric test: $p < 0.05$; 0.1234 (ns), 0.0332 (*), 0.0021 (**), 0.0002 (***), <0.0001 (****), $n = 3$.

preparation. Accordingly with literature, the antioxidant activity showed by thymol-containing materials increased with the phenolic content in a dose-dependent manner (Al-Sheerazee et al., 2024; Kavoosi et al., 2013). Moreover, the antioxidant activity of S-T7+ can help reducing the excess of free radicals present in the wound environment, favouring the healing (Casado-Diaz et al., 2022; Johnson et al., 2022; Schäfer & Werner, 2008).

3.4.6. *Preliminary antimicrobial and antibiofilm tests*

S-Thy, S-T7+, and S-T14+ antimicrobial and antibiofilm activities were tested against *S. aureus* and *P. aeruginosa*. Other than being two strains of clinical concern, they are an important reference to understand the susceptibility of Gram-positive and Gram-negative bacteria to thymol action. The antimicrobial activity was monitored in real-time by means of isothermal microcalorimetry, while the antibiofilm formation activity was determined by CFU counting of the previously detached biofilm formed on the scaffolds. Isothermal microcalorimetry is a highly sensitive technique that allows to determine the scaffolds effects on the metabolic activity of the bacteria, reflecting their viability. The advantage of the technique relies on the precise and continuous monitoring in

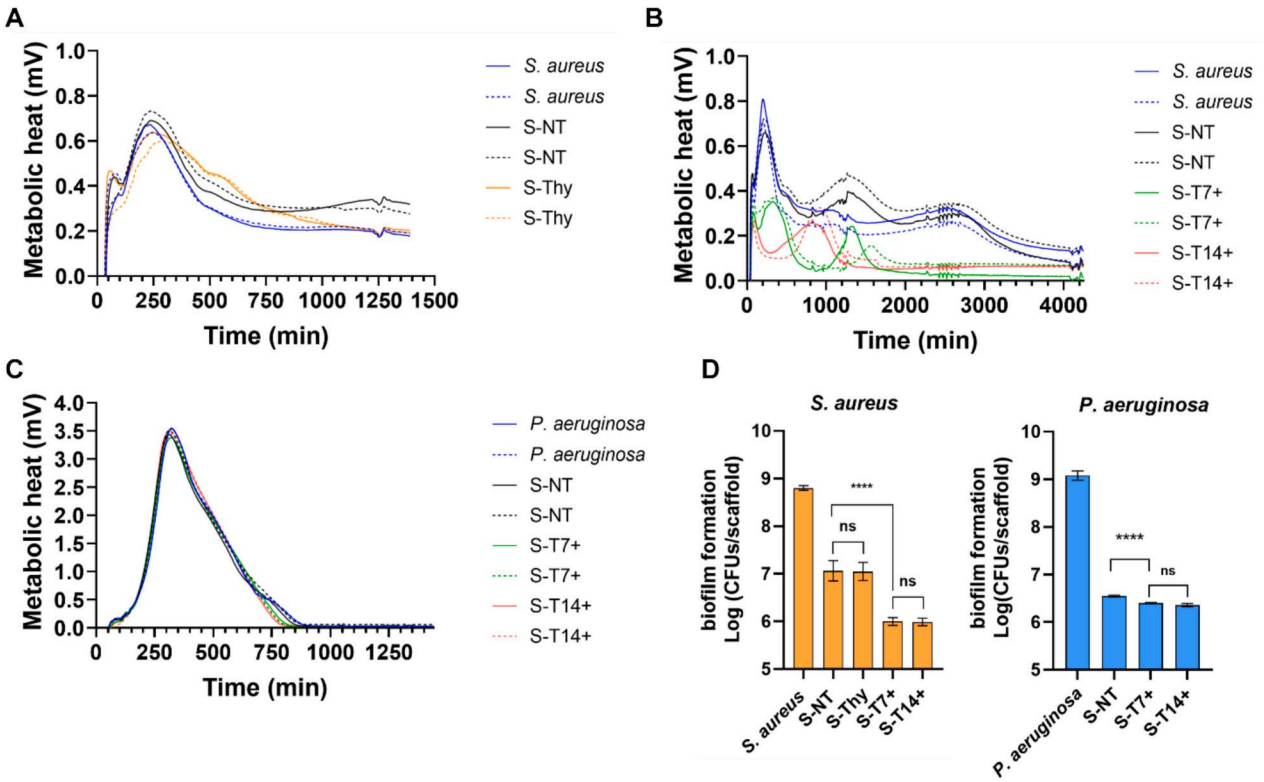

Fig. 8. Isothermal microcalorimetry runs carried out at 37 °C for (A) *S. aureus* (initial O.D. 0.1) cultured in TSB-1 with or without S-NT and S-Thy and monitored for 24 h, (B) *S. aureus* (initial O.D. 0.1) cultured in TSB-1 with or without S-NT, S-T7+, and S-T14+ and monitored for 72 h, (C) *P. aeruginosa* (initial O.D. 0.01) cultured in LB with or without S-NT, S-T7+, and S-T14+ and monitored for 24 h. Two replicates are shown for all microcalorimeter graphs for each condition (solid and dotted lines). D) CFU quantification of *S. aureus* and *P. aeruginosa* biofilm formation on S-NT, S-T7+, and S-T14+ scaffolds. One way ANOVA (with Brown Forsythe, and Shapiro-Willis): $p < 0.05$; 0.1234 (ns), 0.0332 (*), 0.0021 (**), 0.0002 (***), <0.0001 (****), $n = 6$.

real time of the metabolic activity, not requiring further bacteria manipulation and overcoming limitations given by turbidity/colour spectroscopical quantification (Braissant et al., 2015; Butini et al., 2019; Farto-Vaamonde et al., 2022). The scaffolds were firstly immersed in PBS pH 7.4 for 30 min, and then incubated into the bacteria inoculum (3 mL) for a determined time (72 h for *S. aureus* and 24 h for *P. aeruginosa*). The preliminary washing step in PBS pH 7.4 was to have similar amount of thymol that the scaffolds can have after Zn^{2+} loading. It might also mimic the dilution effect caused by the contact of a wound dressing with a highly exudative wound (Seijo-Rabina et al., 2024).

The choice to include also S-T14+ in the tests was made to evaluate how higher thymol content can influence the antimicrobial activity. The results showed that S-Thy did not possess any antimicrobial activity against *S. aureus* when compared with control S-NT and bacteria inoculum (Fig. 8A). Differently, the scaffolds S-T7+ and S-T14+ were able to reduce the *S. aureus* metabolic activity showing a more pronounced effect for S-T14+ (Fig. 8B). Conversely, a 1 Log reduction (90 %) of the biofilm formation was seen for both scaffolds when compared to control S-NT, but also underlining that even with a double concentration of thymol into the scaffolds it was not possible to further reduce the biofilm formation (Fig. 8D). Since no antimicrobial action was seen against *S. aureus* for S-Thy, it was not further tested on *P. aeruginosa*, given the lower susceptibility of Gram-negative to thymol. Neither S-T7+ nor S-T14+ were able to provide a strong antimicrobial and antibiofilm activity against *P. aeruginosa*, showing only slight antibiofilm activity when compared to control. The results are in accordance with previous literature data, in which thymol is able to prevent *S. aureus* ATCC 25923 growth starting from 150 μg/mL, and showing a MIC at 200 μg/mL, and an anti-biofilm activity at ½ MIC concentration (Li et al., 2022; Nostro et al., 2007). Considering the thymol content after washing, and that the scaffolds were immersed into 3 mL of inoculum volume, S-Thy, S-T7+ and S-T14+ can provide a concentration of ~35 μg/mL, ~150 μg/mL and ~ 300 μg/mL. Thus, this explains why S-Thy was not able to produce any effect against *S. aureus*, and why S-T14+ has a more pronounced effect on the metabolic activity reduction than S-T7+. On the other hand, S-T7+ and S-T14+ were both able to provide a thymol content that can reach the minimal biofilm inhibition concentration (MBIC). The susceptibility of *Pseudomonas* species to thymol has been reported to be at 30 mM (4.5 mg/mL), while its ability to inhibit or dismantle the biofilm has been reported at ½ MIC (15 mM) (Walsh et al., 2019). These findings explain the poor antimicrobial activity provided by the scaffolds against *P. aeruginosa*. Considering the results obtained during hemocompatibility, the design of scaffolds able to inhibit *P. aeruginosa* biofilm would imply concentrations that might compromise safety and scaffolds properties.

3.5. Zinc-containing scaffolds production and characterization

After the first battery of tests, the scaffold S-T7+ was identified as the one possessing a good balance between structural and mechanical properties, other than possessing high biocompatibility and incipient antimicrobial and antibiofilm properties. Thus, S-T7+ was selected for the Zn^{2+} loading. To better follow how the Zn^{2+} ions can influence the scaffolds properties and evaluate the effect of the combination between thymol and Zn^{2+}, S-NT scaffold was also loaded with Zn^{2+}. $ZnCl_2$ was chosen as Zn^{2+} supply source because of its high-water solubility and GRAS properties, and the resulting Zn^{2+}-loaded scaffolds were designated as S-TZn (from S-T7+) and S-Zn^{2+} (from S-NT).

Before further proceeding with the antimicrobial testing, the scaffolds were fully characterized to detect any differences with the previously discussed scaffolds.

3.5.1. Zinc-containing scaffolds texturometer compression test

The loading of Zn^{2+} did not alter the mechanical properties of the scaffolds, which proved to withstand the cyclic compression forces with a “sponge-like” behaviour (Fig. S3). The Young’s moduli and the area under the curve values (work) were no significantly different when compared to the non-tuned scaffolds (Fig. 9). This confirmed the used tuning and production procedure was suitable for maintaining the original mechanical properties.

3.5.2. Structural and chemical characterization

The analysis of the height, diameter, and weight of S–Zn and S-TZn revealed the scaffolds kept the original structural parameters, showing intra-group homogeneity (Table S1). SEM images evidenced a 1.20 mm spacing between strands that can create microporosity with good fidelity (Fig. 10A-D), generating tunnels that can allow cell migration and mass-transport as well as promote tissue integration and regeneration (Karageorgiou & Kaplan, 2005). As highlighted by Fig. 10E and I, a massive presence of succinic acid crystals was present on the scaffolds surface, even after the crosslinking process. After washing the scaffolds in 5 mL of DDW for 30 min and freeze-drying, simulating the Zn^{2+} loading, the succinic acid excess was removed from the scaffolds. The same trend was seen for S–Zn and S-TZn scaffolds, confirming that it was possible to remove the crosslinker in excess and load the scaffolds with Zn^{2+} in the same step (Fig. 10G and Fig. 10H). Interestingly, a visible difference was seen between HPβCD/Thy complex containing scaffolds (S-T7+ and S-TZn) when compared to S–Zn. The washing/loading process led to formation of micro-holes in the scaffold’s filaments for S-T7+ and S-TZn, while the same phenomena was not spotted on S–Zn, which showed a surface similar to that of the washed S-NT (Virzì et al., 2024). The micropores formation can be caused by partial release of the HPβCD/Thy complexes during the washing/loading process, accordingly with release studies.

ATR-FTIR spectra of the scaffolds showed the combined typical peaks of XG and GG, presenting an intense C–O stretch at ~1022 cm^{-1}, a O–H bending at ~1645 cm^{-1}, a C–H stretch at ~2915 cm^{-1}, and a broad O–H stretch at ~3300 cm^{-1} (Fig. S5) (Motta et al., 2019; Rafigh et al., 2021). As previously reported, the heat catalyzed crosslinking mediated by succinic acid can lead to an intricate ester bond formation (Virzì et al., 2024). Indeed, a broader peak appeared at ~1710–1720 cm^{-1} in all the tested scaffolds, with a consecutive reduction of the O–H stretch and O–H bending peaks. The spectra of S-Thy did not present any remarked peaks that evidence the presence of thymol, which may be due to its low concentration. Differently, the presence of the HPβCD/Thy complex into S-T7+ and S-T14+ was evidenced by its characteristic peaks at ~2925, 1151, ~1078, ~947, 756, and 704 cm^{-1} (Fig. S5) (C. Sun et al., 2021). Regarding the coordination of Zn^{2+} in S–Zn and S-TZn, the intensity of C=O stretch at ~1720 cm^{-1} was reduced, while the intensity of the peak at ~1628–1630 augmented, due to increased asymmetric COO^- stretching (Fig. S5). This can confirm the interaction of the Zn^{2+} with XG carboxyl oxygens (Ebrahiminezhad et al., 2019; Justi et al., 2021). Moreover, the O–H stretch peak present in S-TZn and S–Zn spectra was more intense and shifted down when compared to S-NT (~3300 cm^{-1} *vs* 3348 cm^{-1}), evidencing an interaction between the O–H and Zn^{2+} (Fig. S5). Similar ATR-FTIR data were reported for polyester fabrics treated with increasing concentration of $ZnCl_2$, showing an increased intensity of the O–H stretch with a consecutive red-shift, and the appearance of a more intense peak around 1618 cm^{-1} (Holt et al., 2018).

3.5.3. Zinc release

Both S–Zn and S-TZn showed a fast release of Zn^{2+} ions when immersed in SWF at 37 °C, by almost releasing all the loaded Zn^{2+} content in the first hours (Fig. 11A and B). Similar release profile was reported for polysaccharides-based materials containing Zinc salts. Indeed, a fast release of Zn^{2+} ions was recorded from a commercially available over-the-counter zinc-containing vaginal gel, based on hydroxyethyl cellulose and zinc sulfate, reaching the maximum release level at 30 min *in vitro* (Fenyvesi et al., 2020). Similarly, $ZnCl_2$-containing chitosan fibers were shown to rapidly release the loaded zinc in 1 h (Qin et al., 2006).

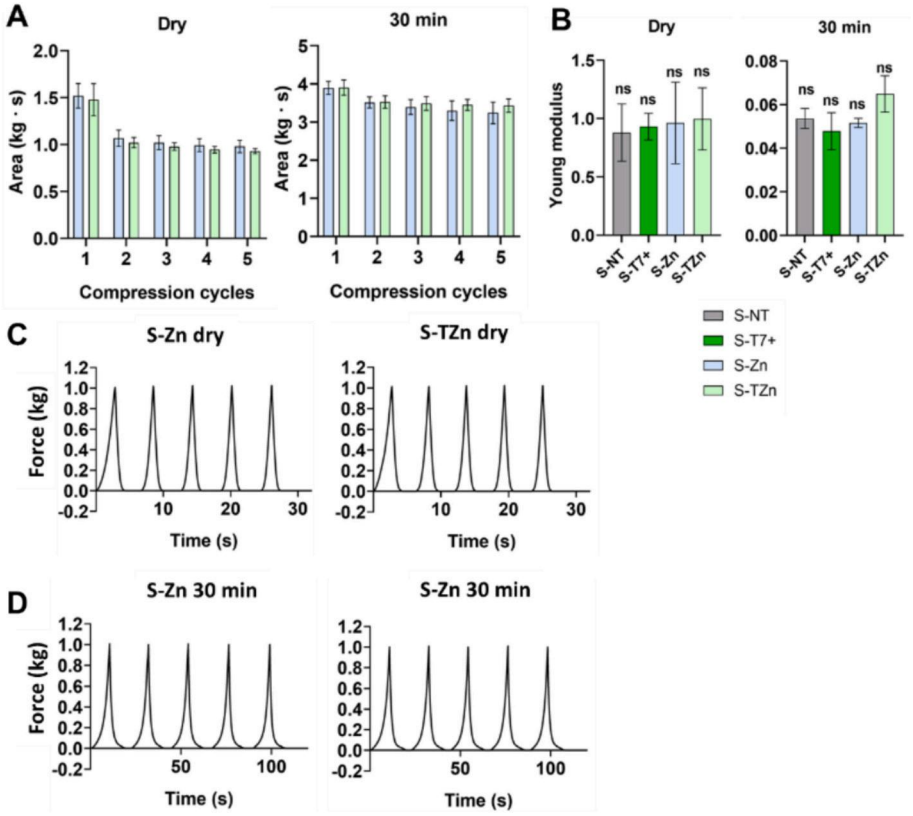

Fig. 9. A) Area under the curve (work) values after five consecutive compressions cycles for dry S–Zn, and S-TZn scaffolds, and swelled in DDW for 30 min. B) Calculated Young modulus for scaffolds S-NT, S-T7+, S–Zn, and S-TZn in dry and wet (30 min swelling) conditions. Mechanical behaviour recorded for scaffolds when subjected to five consecutive compression/decompression forces of 1 kg: dried scaffolds (C) and after being immersed in PBS pH 7.4 for 30 min (D). Kruskal-Wallis non-parametric test: $p < 0.05$; 0.1234 (ns), 0.0332 (*), 0.0021 (**), 0.0002 (***), <0.0001 (****), $n = 3$.

The presence of the HPβCD/Thy in S-TZn did not influence Zn^{2+} loading and release process, showing no significant differences in the total loaded and released amount between S-TZn and S–Zn (Fig. 11A). In parallel, the release of the remaining amount of thymol present in S-TZn was analyzed (Fig. 11C). The data reported a residual amount of ~50 % HPβCD/Thy after the loading of Zn^{2+}, matching with the preliminary data reported on S-T7+ release in PBS pH 7.4 (Fig. 6). Even in this case, all the thymol was released during the first hours. The Zn^{2+} and thymol burst release profile can provide antibacterial and antibiofilm scaffolds activity. Indeed, it is necessary to rapidly reach a concentration able to inhibit, stop, or mitigate the bacterial infection and the formation of biofilm to achieve suitable effects.

3.5.4. Zinc-containing scaffolds antimicrobial and antibiofilm tests

After the Zn^{2+} loaded scaffolds characterization, their antimicrobial and antibiofilm properties were evaluated. A preliminary screening was performed in MHA-1 agar plates to challenge S-TZn and S–Zn against *S. aureus*, *P. aeruginosa*, *S. epidermidis*, and *E. coli* (Fig. S6). The results evidenced the formation of a inhibition halo around the scaffolds (Fig. S6) which, considering the limited diffusion that Zn^{2+} and thymol can have in the agar plates, indicated the susceptibility of all the tested bacteria to Zn^{2+}. Thus, further antimicrobial studies were conducted by means of microcalorimetry and biofilm viable cell counting, as previously reported for S-T7+. The tests were conducted on *S. aureus*, *P. aeruginosa*, and *S. epidermidis* which, differently from most of the laboratory *E. coli* strains, are usually recognized also as massive biofilm producer strains (Beloin et al., 2008). The obtained data underlined the ability of the S-TZn and S–Zn scaffolds to markedly reduce the metabolic heat of *S. aureus* and *S. epidermidis* when compared to controls (bacteria alone or in contact with S-NT), while the reduction was less marked for *P. aeruginosa* (Fig. 12A). Indeed, in the latter case a moderate antibacterial effect was observed in the descendent part of the metabolic heat curve, showing a ~ 2.5 h reduction before the controls. The presence of thymol in S-TZn did not lead to a notably higher antimicrobial activity when compared to S–Zn against *P. aeruginosa* (Fig. 12A). Differently, a significant difference was seen for the antibiofilm activity against Gram-positive strains when both thymol and Zn^{2+} were combined, showing a stronger antibiofilm (Fig. 12B and Fig. S7). Indeed, against *S. aureus* S–Zn led to a ~ 2.9 Log (99.87 %) reduction of biofilm formation, while S-TZn presented a ~ 3.3 Log (99.95 %) reduction. The same tendency was seen in *S. epidermidis*, where a Log reduction of 1.16 was seen for S–Zn (93.08 %), while the reduction was of 1.76 Log (98.26 %) for S-TZn. Interestingly, no significant differences were seen in reduction of *P. aeruginosa* biofilm formation, giving a Log reduction of 3.76 (99.98 %) and 3.91 (99.99 %) for S–Zn and S-TZn, respectively. These data were in agreement with the previous tests (Fig. 8), confirming that Gram-positive bacteria such as *S. aureus* are more susceptible to thymol antimicrobial and antibiofilm effect. Conversely, the strong antibiofilm properties showed by the scaffolds against *P. aeruginosa* was attributable only to Zn^{2+}.

Previously reported antimicrobial broth dilution method results highlighted the susceptibility of *S. aureus* strains to $ZnCl_2$ for both planktonic and biofilm form, in concentrations ranging from 0.9 to 2 mM. For *P. aeruginosa* strains, the preventive biofilm concentration was 4.0 mM, and no MIC or MBC values were found at the tested concentrations. However, a significant decrease of the biofilm formation was reported for the $ZnCl_2$-coated splints in comparison with the non-coated splints for both *S. aureus* and *P. aeruginosa* (Noach et al., 2023). Moreover, polyester textiles treated with 50 mM, 100 mM, and 500 mM of $ZnCl_2$ were shown to avoid any bacteria contamination of the fabrics when exposed to contaminated environments and surfaces (Holt et al., 2018). Similarly, porous metal zinc scaffolds were shown to completely

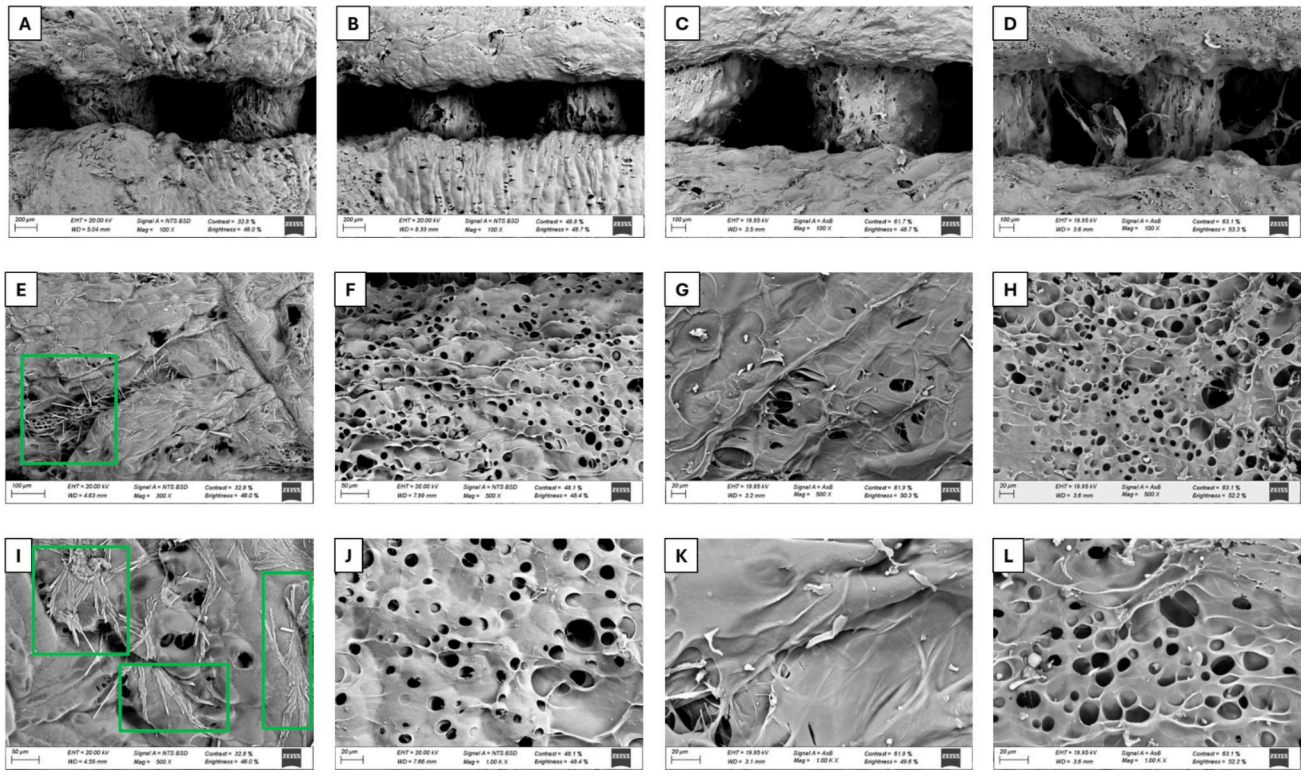

Fig. 10. A) S-T7+ scaffold before washing in DDW (top view, 100×); B) S-T7+ scaffold after washing in DDW for 30 min and freeze dried (top view, 100×); C) S–Zn scaffolds (top view, 100×); D) S-TZn scaffolds (top view, 100×); E) S-T7+ scaffold before washing in DDW, the succinic acid crystals are highlighted by the green square (top view, 300×); F) S-T7+ scaffold after washing in DDW for 30 min and freeze dried (top view, 300×); G) S–Zn scaffolds (top view, 300×); H) S-TZn scaffolds (top view, 300×); I) S-T7+ scaffold before washing in DDW, the succinic acid crystals are highlighted by the green squares (top view. 500×); J) S-T7+ scaffold after washing in DDW for 30 min and freeze dried (top view, 1000×); K) S–Zn scaffolds (top view, 1000×); L) S-TZn scaffolds (top view, 1000×).

inhibit *S. aureus* and *E. coli* biofilm formation on their surface (Cockerill et al., 2020).

3.5.5. *Zinc scaffolds biocompatibility tests*

Given the potent antibiofilm and antibacterial activity showed by the scaffolds, further investigations were done to assess their biocompatibility. The tested scaffolds showed high hemocompatibility, reporting similar results to negative control (NaCl 0.9 % *v*/v) (Fig. 13A). Moreover, also pure $ZnCl_2$ solution did not cause relevant hemolysis even at the highest concentration tested (100 mM) (Fig. S4) in good agreement with previous reports on Zn alloys and zinc-embedding composites (Fenyvesi et al., 2020).

On the other hand, some clarifications are required for the correct *in vitro* testing of Zn^{2+} containing biomaterials. Even if Zn^{2+} ions (as well as $ZnCl_2$) are widely recognized as safe for human use and their medicinal use is approved and accepted (Food and Drug Administration, 1986) Zn^{2+} salts and ions can have a strong toxic effect during *in vitro* tests, limiting the correct cytocompatibility testing for this GRAS material (Salesa et al., 2021). Consistently, Cockerill et al. already highlighted the limitation for direct *in vitro* testing of zinc containing scaffolds, claiming that classic *in vitro* cytocompatibility tests did not reflect what could happen *in vivo* (Cockerill et al., 2020). Indeed, the wound is a dynamic system, in which the production of exudates and cell migration should be taken into account for a more accurate mimicking during *in vitro* testing. A wound infected by *S. aureus* generally produces 2.8 mL/cm^2/24 h, which corresponds to a 0.116 μL/cm^2/h exudate production (Dealey et al., 2006). To simulate the arrival of new cells during wound healing, the fresh media contained a cell density of 60,000 cells/mL. The initial cell density was of 40,000 cells/well. The performed "dynamic" test evidenced a much higher fluorescence intensity for cells treated with Zn^{2+} than the initial cell amount (I.C.V.) (Fig. 13B and C) before and after 24 h in culture, demonstrating that the supply of new media and cells can regenerate eventual toxic effect given by Zn^{2+} under static conditions. It should be noted that the I.C.V. was measured with Alamar blue, which directly measures the metabolic activity, and specifically the reducing power, of the viable cells. A maximum cell viability was seen for S-NT, where no toxic effects were evidenced when compared to the zinc containing scaffolds. Anyway, in the worst-case scenario, even if Zn^{2+} may lack in selectivity, causing indiscriminately toxic effect to bacteria and human cells, new cells supply can conquer the treated wound site, restoring the initial conditions or start regenerating it. Furthermore, after exerting its antibacterial and antibiofilm contribution, Zn^{2+} can be reabsorbed, reused, and/or cleared by the human body without leading to any systemic toxic effects. Accordingly, several studies exemplified Zinc composites high biocompatibility *in vivo*. Indeed, pure zinc stent have shown an excellent biocompatibility, even after degradation, reporting no severe inflammation, platelet aggregation, thrombosis, or hyperplasia when implanted into the abdominal aorta of rabbits for 12 months (Yang et al., 2017). Similar reports were described for Zn–Li alloy implanted in rats (Zhao et al., 2017). Moreover, Cur/ZnO/PVA nanofibers dressing demonstrated high biocompatibility and promoted cell proliferation *in vivo*, significantly accelerating wound healing (Nemati et al., 2024).

3.5.6. *In ovo zinc scaffolds tissue integration and angiogenesis evaluation*

Finally, the ability of the produced scaffolds to promote tissue integration and angiogenesis was studied by means of an *in ovo* CAM test to verify that the antimicrobial tuning did not alter the tissue integration and angiogenetic properties of the S-NT scaffolds (Virzì et al., 2024). Indeed, thanks to angiogenesis and novel microvasculature formation, it can be possible to re-establish an adequate exchange of nutrients, cells, oxygen, growth factors, and waste products, facilitating wound recovery

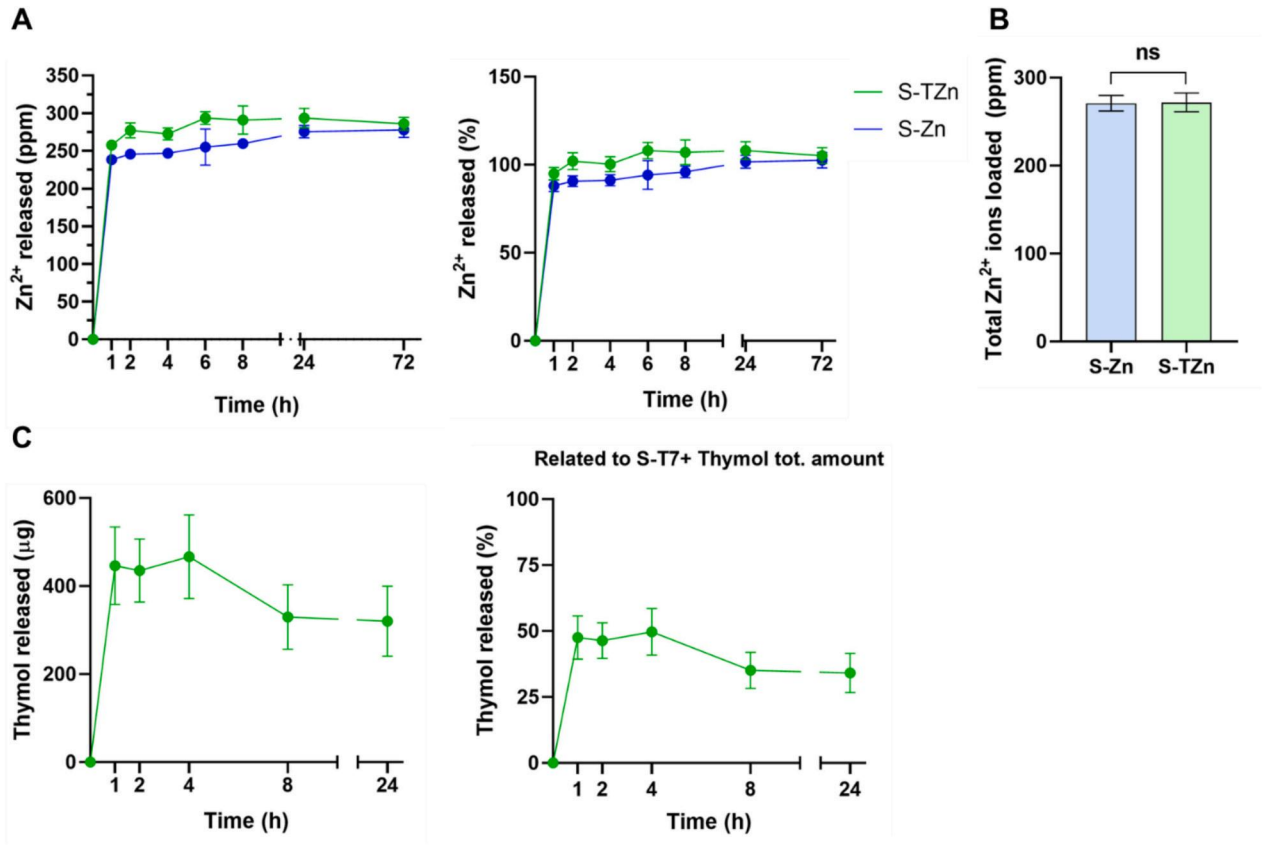

Fig. 11. A) Zn^{2+} release from scaffolds S–Zn and S-TZn conducted in SWF at 37 °C, 100 osc/min; B) Total amount of Zn^{2+} loaded into S–Zn and S-TZn quantified by ICP-OES after immersing the scaffolds in 10 mL of SWF for 72 h at 37 °C and 100 osc/min. C) Thymol release from the scaffold S-TZn conducted in SWF at 37 °C, 100 osc/min. Unpaired *t*-test with Welch's correction: $p < 0.05$; 0.1234 (ns), 0.0332 (*), 0.0021 (**), 0.0002 (***), <0.0001 (****), $n = 3$.

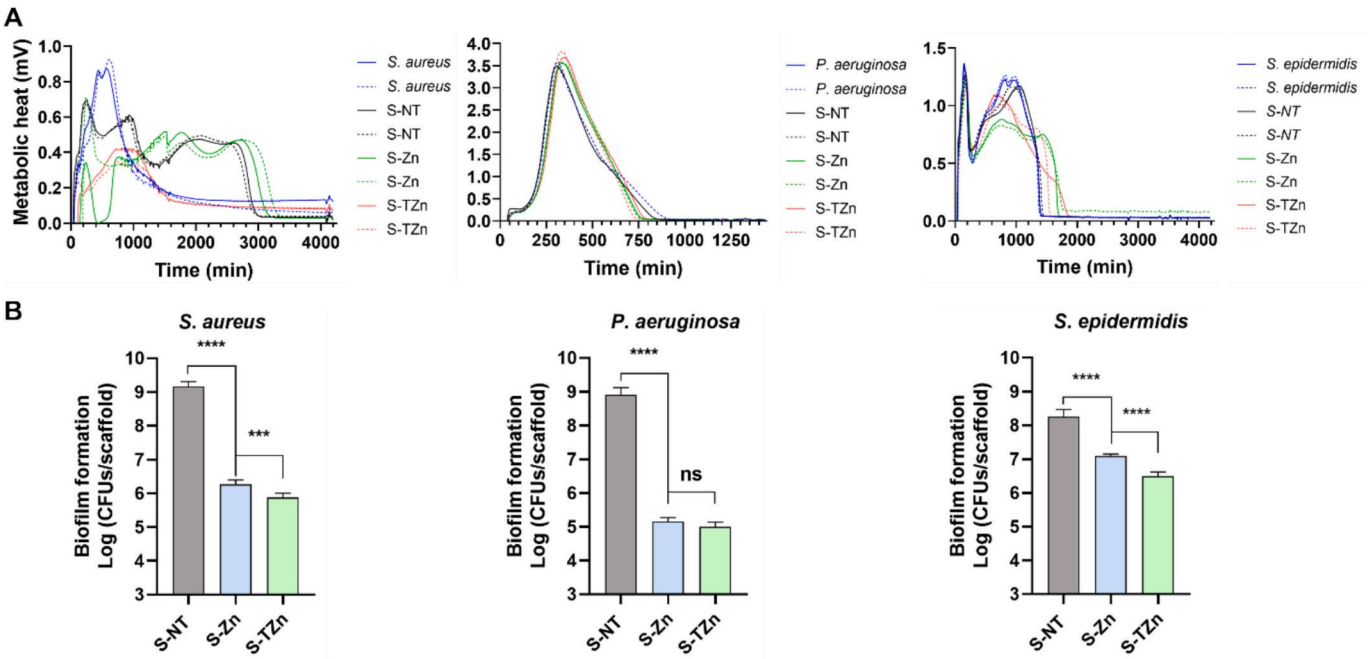

Fig. 12. A) Microcalorimeter graphs of S-NT, S–Zn, and S-TZn scaffolds against *S. aureus*, *P. aeruginosa*, and *S. epidermidis*. B) CFU quantification of *S. aureus*, *P. aeruginosa*, and *S. epidermidis* biofilms formation on S-NT, S–Zn, and S-TZn scaffolds (n = 3). One way ANOVA (with Brown Forsythe, and Shapiro-Willis): $p < 0.05$; 0.1234 (ns), 0.0332 (*), 0.0021 (**), 0.0002 (***), <0.0001 (****), $n = 6$.

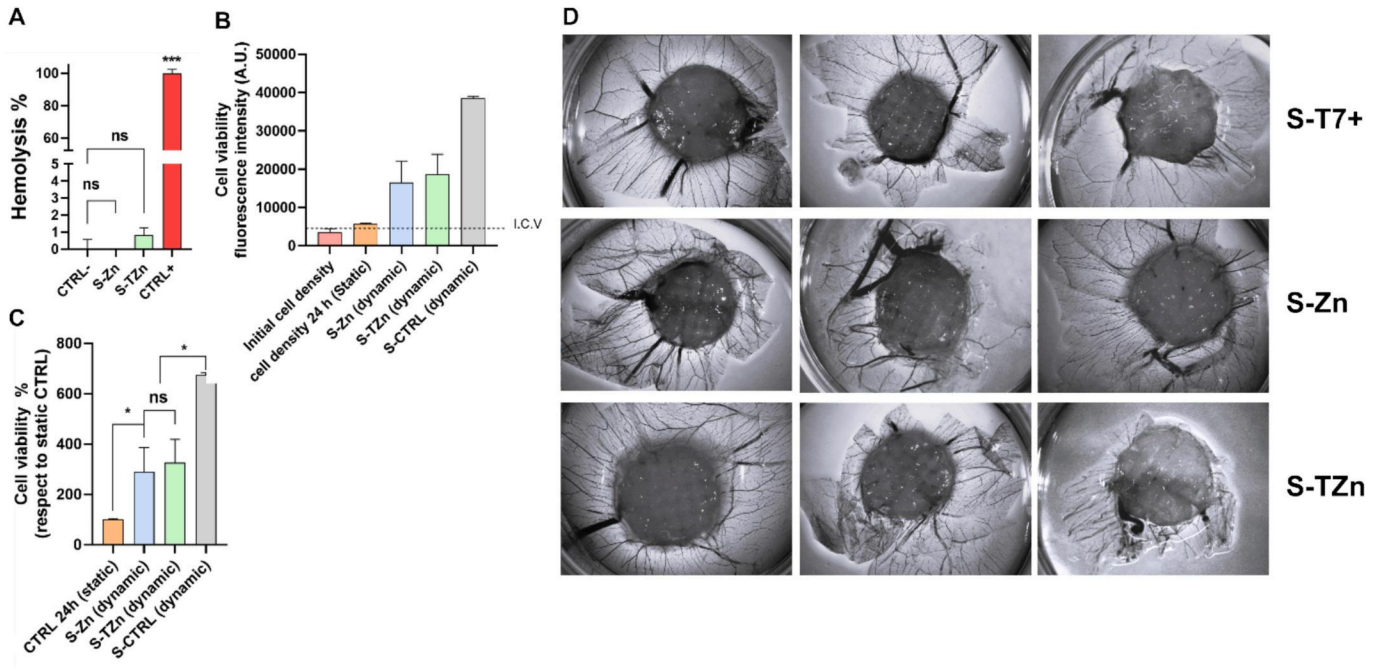

Fig. 13. A) Hemolytic effect of scaffolds S-NT, S-T7+, S–Zn, and S-TZn, CTRL – was NaCl 0.9 % *w/v*, CTRL + was Triton-X 4 % v/v; B) *In vitro* dynamic cytocompatibility test results: I.C.V was initial cell viability, the scaffold of control (S-CTRL) was S-NT, the cell density after 24 h was the initial cell density cultured in "static" for 24 h; C) Cell viability compared to initial cell density cultured in "static" conditions for 24 h (CTRL 24 h); D) Images of the resected CAM integrated with the S-T7+, S–Zn, and S-TZn scaffolds. The image acquisitions were made using an Olympus SZ-CTV stereomicroscope using black and white filter to contrast vessels and scaffolds. One way ANOVA (with Brown Forsythe, and Shapiro-Willis): $p < 0.05$; 0.1234 (ns), 0.0332 (*), 0.0021 (**), 0.0002 (***), <0.0001 (****), n = 6.

(Veith et al., 2019).

The *in ovo* CAM test is a low cost, reliable, and reproducible alternative to *in vivo* studies, and can be helpful in reducing, refining, and replacing animals in preclinical testing, according to the European Chemical Agency (ECHA) recommendation (Farto-Vaamonde et al., 2022). Indeed, it is not considered an animal experiment under Directive 2010/63/EU, because no nervous system is developed before embryonal day (ED) 11, and a chick embryo does not suffer pain until ED 14 (since the chorioallantoic membrane is not innervated). Moreover, according to the Institutional Animal Care and Use Committee (IACUC) and the USA National Institutes of Health the embryo is not considered as a living animal until ED 17 (Directive EU 2010/63, 2010; Kundeková et al., 2021).

As previously reported, doses of 150–250 μg Zn/egg can have a toxic effect for the embryos during *in ovo* testing (Sun et al., 2018). Indeed, the Zn content present in the eggs themselves is already adequate for correct embryonic development, and a supply of higher Zn^{2+} can create an imbalance that can be harmful to embryonic development (Oliveira et al., 2015; Sun et al., 2018), resulting in false negatives results. For the presented reasons, the scaffolds were tested after being soaked in PBS pH 7.4 for 24 h to release the Zn^{2+} ions, and to evidence the capacity of the scaffolds to be integrated into the CAM and maintain their angiogenetic and wound healing effect, mimicking what can happen after the antimicrobial effect.

A macroscopic visual and histological analysis of the eggs revealed that the scaffolds showed no toxic or hemolytic effect, evidencing very good adherence and integration (integration score: 3) into the CAM, presenting microcapillary and vessels development around the scaffolds' structure (Fig. 13D). Thus, these data revealed that the tuning process did not alter the wound healing capacity of the XG/GG based scaffolds (Fig. 13D).

4. Conclusions

In the present work XG/GG-based scaffolds were tuned with thymol and Zn^{2+} to prepare medical devices possessing antibiofilm and antimicrobial properties while maintaining intrinsic wound healing ability. HPβCD efficiently endowed the scaffolds with the capability to host the natural compound thymol, while the polysaccharides themselves hosted the divalent metal ions, thus providing complementary mechanisms to prevent biofilm formation as hypothesized. HPβCD/Thy complexes allowed loading the scaffolds with a higher content of thymol, mitigating the thymol hemolytic effect and yielding higher antioxidant activity. Texturometer compression tests highlighted the tuning process did not compromise the mechanical properties of S-T7+, S-TZn, and S–Zn scaffolds, which possessed similar behaviour to the non-tuned XG/GG scaffolds (S-NT). The final Zn^{2+}-loaded scaffolds (S-TZn and S–Zn) demonstrated enhanced antimicrobial properties compared to S-T7+, showing potent antibiofilm activity on both Gram-positive and Gram-negative strains of clinical interest. The concomitant presence of thymol and Zn^{2+} in S-TZn led to more potent antibiofilm activity against Gram-positive bacteria such as *S. aureus* and *S. epidermidis* when compared to S–Zn, while no differences were observed for *P. aeruginosa.* Even considering the limitations of *in vitro* testing of Zn^{2+}-containing biomaterials, S-TZn and S–Zn displayed high hemocompatibility, while the "dynamic" *in vitro* test and the *in ovo* CAM test demonstrated the beneficial advantages of using the Zn^{2+}-embedding scaffolds. Indeed, after exploiting their antibiofilm and antimicrobial effect, the scaffolds can assist in wound healing, promoting tissue integration and angiogenesis.

Thus, the described 3D-printed porous scaffold S-TZn and S–Zn, in addition to being an eco-sustainable and green alternative to non-biodegradable synthetic based medical devices, proved to be able to combine the wound healing effect of the unmodified scaffold with a potent antibiofilm and antimicrobial effect given by thymol and Zn^{2+}. Furthermore, the combination of thymol and Zn^{2+} demonstrated that it could be helpful in fighting the development of antimicrobial resistance.

The present study represents a significant advancement in polysaccharide science and technology by integrating the multifunctional characteristics of polysaccharides (such as antibiofilm prevention, drug

delivery, and wound healing capabilities) together with advanced 3D printing techniques into the design of scaffolds. The correct selection of polysaccharide blends to be used as 3D printing inks opens up a wide range of possibilities in obtaining biomaterials tailored to specific therapeutic needs. This innovation not only broadens the biomedical applications of polysaccharides but also supports the creation of personalized medical devices for wound healing, taking into account also antimicrobial resistances. The successful SSE 3D printing production approach and material composition may be an inspiration for future designs of non-plastic therapeutic materials, capable of exploiting natural compounds and metal ion delivery for wound healing and infection control. The developed scaffolds overcome key limitations of the production and use of polysaccharide-based 3D printed composites, such as poor rheological properties of inks, limited resolution and structural features, low capacity to incorporate hydrophobic active substances, and inadequate mechanical strength of 3D printed materials. Indeed, the study provides a comprehensive characterization and testing approach to ensure that these scaffolds not only meet structural and mechanical requirements but also exhibit effective therapeutic and biocompatibility properties. The use of isothermal microcalorimetry for antibacterial and antibiofilm testing, coupled with a dynamic *in vitro* model simulating wound healing, may inspire future researchers to advance alternative methods to animal testing for antibacterial wound material assessment. The promising *in vitro* and *in ovo* results suggest that these tuned XG/GG scaffolds could be valuable candidates for further *in vivo* studies.

CRediT authorship contribution statement

Nicola Filippo Virzì: Writing – review & editing, Writing – original draft, Visualization, Validation, Software, Methodology, Investigation, Formal analysis, Data curation, Conceptualization. **Patricia Diaz-Rodriguez:** Writing – review & editing, Visualization, Validation, Supervision, Methodology, Investigation, Data curation, Conceptualization. **Angel Concheiro:** Writing – review & editing, Resources, Project administration, Funding acquisition, Conceptualization. **Ana Otero:** Writing – review & editing, Resources, Methodology, Data curation, Conceptualization. **Antonino Mazzaglia:** Writing – review & editing, Supervision, Methodology, Investigation, Conceptualization. **Valeria Pittalà:** Writing – review & editing, Writing – original draft, Supervision, Resources, Project administration, Investigation, Funding acquisition. **Carmen Alvarez-Lorenzo:** Writing – review & editing, Writing – original draft, Supervision, Resources, Project administration, Methodology, Investigation, Funding acquisition, Conceptualization.

Funding

The work was supported by Spain Ministerio de Ciencia e Innovación MCIN/AEI/10.13039/501100011033 [PID2023-150422OB-I00], Xunta de Galicia [ED431C 2024/09], FEDER, and Italian PON Project BONE++ Development of Micro and Nanotechnologies for Predictivity, Diagnosis, Therapy and Regenerative Treatments of Pathological Bone and Osteo-Articular Alterations [ARS01_00693]. Work partially financed by project IBEROS+ [0072_IBEROS_MAIS_1_E] Interreg-POCTEP 2021–2027.

Declaration of competing interest

The authors declare that they have no known competing financial interests or personal relationships that could have appeared to influence the work reported in this paper.

Acknowledgements

The authors wish to thank Rubén Corral Aneiros and Alfredo Rodríguez Carreira of the Institute of Materials of the University of Santiago de Compostela (iMATUS) for the technical support on ICP-OES analysis.

Appendix A. Supplementary data

Supplementary data to this article can be found online at https://doi.org/10.1016/j.carbpol.2024.123069.

Data availability

Data will be made available on request.

References

Ahmad, N. (2023). In vitro and in vivo characterization methods for evaluation of modern wound dressings. *Pharmaceutics, 15*(1), 42.
Ahmady, A. R., Razmjooee, K., Saber-Samandari, S., & Toghraie, D. (2022). Fabrication of chitosan-gelatin films incorporated with thymol-loaded alginate microparticles for controlled drug delivery, antibacterial activity and wound healing: In-vitro and in-vivo studies. *International Journal of Biological Macromolecules, 223*(Pt A), 567–582.
Al-Sheerazee, N. M. M. B., Özgen, S., & Özbaş, Z. (2024). Development of thymol-loaded polymeric films designed as wound dressing materials: Physical, antioxidant, antibacterial, cytocompatibility, and wound healing properties. *Journal of Drug Delivery Science and Technology, 97*, Article 105744.
Alvarez Echazú, M. I., Olivetti, C. E., Anesini, C., Perez, C. J., Alvarez, G. S., & Desimone, M. F. (2017). Development and evaluation of thymol-chitosan hydrogels with antimicrobial-antioxidant activity for oral local delivery. *Materials Science & Engineering. C, Materials for Biological Applications, 81*, 588–596.
Beloin, C., Roux, A., & Ghigo, J. M. (2008). *Escherichia coli* biofilms. *Current Topics in Microbiology and Immunology, 322*, 249–289.
Bouhrour, N., Nibbering, P. H., & Bendali, F. (2024). Medical device-associated biofilm infections and multidrug-resistant pathogens. *Pathogens, 13*(5), 393.
Braissant, O., Bachmann, A., & Bonkat, G. (2015). Microcalorimetric assays for measuring cell growth and metabolic activity: Methodology and applications. *Methods, 76*, 27–34.
Butini, M. E., Abbandonato, G., Di Rienzo, C., Trampuz, A., & Di Luca, M. (2019). Isothermal microcalorimetry detects the presence of persister cells in a Staphylococcus aureus biofilm after vancomycin treatment. *Frontiers in Microbiology, 10*, 332.
Casado-Diaz, A., Moreno-Rojas, J. M., Verdú-Soriano, J., Lázaro-Martínez, J. L., Rodríguez-Mañas, L., Tunez, I., … Pereira-Caro, G. (2022). Evaluation of antioxidant and wound-healing properties of EHO-85, a novel multifunctional amorphous hydrogel containing *Olea europaea* leaf extract. *Pharmaceutics, 14*(2).
Castillo, A., Celeiro, M., Lores, M., Grgić, K., Banožić, M., Jerković, I., & Jokić, S. (2023). Bioprospecting of targeted phenolic compounds of *Dictyota dichotoma, Gongolaria barbata, Ericaria amentacea, Sargassum Hornschuchii* and *Ellisolandia elongata* from the Adriatic Sea extracted by two green methods. *Marine Drugs, 21*(2).
Celebioglu, A., Yildiz, Z. I., & Uyar, T. (2018). Thymol/cyclodextrin inclusion complex nanofibrous webs: Enhanced water solubility, high thermal stability and antioxidant property of thymol. *Food Research International, 106*, 280–290.
Chen, M., Yu, Q., & Sun, H. (2013). Novel strategies for the prevention and treatment of biofilm related infections. *International Journal of Molecular Sciences, 14*(9), 18488–18501.
Cockerill, I., Su, Y., Sinha, S., Qin, Y. X., Zheng, Y., Young, M. L., & Zhu, D. (2020). Porous zinc scaffolds for bone tissue engineering applications: A novel additive manufacturing and casting approach. *Materials Science & Engineering. C, Materials for Biological Applications, 110*, Article 110738.
Coma, V., Sebti, I., Pardon, P., Pichavant, F. H., & Deschamps, A. (2003). Film properties from crosslinking of cellulosic derivatives with a polyfunctional carboxylic acid. *Carbohydrate Polymers, 51*(3), 265–271.
Conceição, J., Farto-Vaamonde, X., Goyanes, A., Adeoye, O., Concheiro, A., Cabral-Marques, H., … Alvarez-Lorenzo, C. (2019). Hydroxypropyl-β-cyclodextrin-based fast dissolving carbamazepine printlets prepared by semisolid extrusion 3D printing. *Carbohydrate Polymers, 221*, 55–62.
Costa, M. F., Durço, A. O., Rabelo, T. K., Barreto, R. S. S., & Guimarães, A. G. (2019). Effects of carvacrol, thymol and essential oils containing such monoterpenes on wound healing: A systematic review. *The Journal of Pharmacy and Pharmacology, 71*(2), 141–155.
Dealey, C., Cameron, J., & Arrowsmith, M. (2006). A study comparing two objective methods of quantifying the production of wound exudate. *Journal of Wound Care, 15*(4), 149–153.
Depypere, M., Morgenstern, M., Kuehl, R., Senneville, E., Moriarty, T. F., Obremskey, W. T., … Metsemakers, W. J. (2020). Pathogenesis and management of fracture-related infection. *Clinical Microbiology and Infection, 26*(5), 572–578.
Directive EU 2010/63 of the European Parliament and of the Council of 22 September 2010 on the Protection of Animals Used for Scientific Purposes. (2010). *European Union, Belgium, Brussels* (pp. 1–47).
Duan, Y., Li, K., Wang, H., Wu, T., Zhao, Y., Li, H., … Yang, W. (2020). Preparation and evaluation of curcumin grafted hyaluronic acid modified pullulan polymers as a functional wound dressing material. *Carbohydrate Polymers, 238*, Article 116195.
Ebrahiminezhad, A., Moeeni, F., Taghizadeh, S.-M., Seifan, M., Bautista, C., Novin, D., … Berenjian, A. (2019). Xanthan gum capped ZnO microstars as a promising dietary zinc supplementation. *Foods, 8*(3), 88.

Farani, M., & Shafiee, A. (2021). Wound healing: From passive to smart dressings. *Advanced Healthcare Materials, 10*, Article 2100477.
Farto-Vaamonde, X., Diaz-Gomez, L., Parga, A., Otero, A., Concheiro, A., & Alvarez-Lorenzo, C. (2022). Perimeter and carvacrol-loading regulate angiogenesis and biofilm growth in 3D printed PLA scaffolds. *Journal of Controlled Release, 352*, 776–792.
Fenyvesi, F., Váradi, J., Fehér, P., Bácskay, I., Vecsernyés, M., Sipos, A., & Takacs, P. (2020). Biocompatibility and zinc release testing of a zinc-containing vaginal gel. *Menopause, 27*(2), 143–149.
Food and Drug Administration. (1986). https://www.accessdata.fda.gov/scripts/cder/daf/index.cfm?event=overview.process&applno=018959 Accessed September 15 2024.
Frei, A., Verderosa, A. D., Elliott, A. G., Zuegg, J., & Blaskovich, M. A. T. (2023). Metals to combat antimicrobial resistance. *Nature Reviews Chemistry, 7*(3), 202–224.
Gabbai-Armelin, P. R., Sales, L. S., Ferrisse, T. M., De Oliveira, A. B., De Oliveira, J. R., Giro, E. M. A., & Brighenti, F. L. (2022). A systematic review and meta-analysis of the effect of thymol as an anti-inflammatory and wound healing agent: A review of thymol effect on inflammation and wound healing. *Phytotherapy Research, 36*(9), 3415–3443.
Garg, A., Ahmad, J., & Hassan, M. Z. (2021). Inclusion complex of thymol and hydroxypropyl-β-cyclodextrin (HP-β-CD) in polymeric hydrogel for topical application: Physicochemical characterization, molecular docking, and stability evaluation. *Journal of Drug Delivery Science and Technology, 64*, Article 102609.
Gbejuade, H. O., Lovering, A. M., & Webb, J. C. (2015). The role of microbial biofilms in prosthetic joint infections. *Acta Orthopaedica, 86*(2), 147–158.
Ghorpade, V. S., Yadav, A. V., & Dias, R. J. (2017). Citric acid crosslinked β-cyclodextrin/carboxymethylcellulose hydrogel films for controlled delivery of poorly soluble drugs. *Carbohydrate Polymers, 164*, 339–348.
Górecki, A., & Babiak, I. (2009). Infection of joint prosthesis and local drug delivery. In H. Kienapfel, & K.-D. Kühn (Eds.), *The infected implant* (pp. 19–26). Berlin, Heidelberg: Springer Berlin Heidelberg.
Hassanisaadi, M., Vatankhah, M., Kennedy, J. F., Rabiei, A., & Saberi Riseh, R. (2025). Advancements in xanthan gum: A macromolecule for encapsulating plant probiotic bacteria with enhanced properties. *Carbohydrate Polymers, 348, Part A*, Article 122801.
Hollow, S. E., & Johnstone, T. C. (2022). Encapsulation of closo-dodecaiododecaborate in 2-hydroxypropyl-γ-cyclodextrin prevents hemolysis†. *Chemical Communications, 58*(14), 2375–2378.
Holt, B. A., Gregory, S. A., Sulchek, T., Yee, S., & Losego, M. D. (2018). Aqueous zinc compounds as residual antimicrobial agents for textiles. *ACS Applied Materials & Interfaces, 10*(9), 7709–7716.
Johnson, J. B., Broszczak, D. A., Mani, J. S., Anesi, J., & Naiker, M. (2022). A cut above the rest: Oxidative stress in chronic wounds and the potential role of polyphenols as therapeutics. *The Journal of Pharmacy and Pharmacology, 74*(4), 485–502.
Justi, M., Puggina, M., Silla, J. M., Nunes, C. A., & Silva, C. A. (2021). Molecular structure features and fast identification of chemical properties of metal carboxylate complexes by FTIR and partial least square regression. *Journal of Molecular Structure, 1237*, Article 130405.
Kang, X., Yang, X., He, Y., Guo, C., Li, Y., Ji, H., … Wu, L. (2023). Strategies and materials for the prevention and treatment of biofilms. *Materials Today Bio, 23*, Article 100827.
Karageorgiou, V., & Kaplan, D. (2005). Porosity of 3D biomaterial scaffolds and osteogenesis. *Biomaterials, 26*(27), 5474–5491.
Kavoosi, G., Dadfar, S. M., & Purfard, A. M. (2013). Mechanical, physical, antioxidant, and antimicrobial properties of gelatin films incorporated with thymol for potential use as nano wound dressing. *Journal of Food Science, 78*(2), E244–E250.
Khatoon, Z., McTiernan, C. D., Suuronen, E. J., Mah, T. F., & Alarcon, E. I. (2018). Bacterial biofilm formation on implantable devices and approaches to its treatment and prevention. *Heliyon, 4*(12), Article e01067.
Kowalczyk, A., Przychodna, M., Sopata, S., Bodalska, A., & Fecka, I. (2020). Thymol and thyme essential oil—New insights into selected therapeutic applications. *Molecules, 25*(18), 4125.
Kundeková, B., Máčajová, M., Meta, M., Čavarga, I., & Bilčík, B. (2021). Chorioallantoic membrane models of various avian species: Differences and applications. *Biology (Basel), 10*(4).
Kuo, S. H., Shen, C. J., Shen, C. F., & Cheng, C. M. (2020). Role of pH value in clinically relevant diagnosis. *Diagnostics (Basel), 10*(2), 107.
Laurano, R., Boffito, M., Ciardelli, G., & Chiono, V. (2022). Wound dressing products: A translational investigation from the bench to the market. *Engineered Regeneration, 3*, 182–200.
Lavanya, K., Balagangadharan, K., Chandran, S. V., & Selvamurugan, N. (2023). Chitosan-coated and thymol-loaded polymeric semi-interpenetrating hydrogels: An effective platform for bioactive molecule delivery and bone regeneration in vivo. *Biomaterials Advances, 146*, Article 213305.
Li, Q., Huang, K. X., Pan, S., Su, C., Bi, J., & Lu, X. (2022). Thymol disrupts cell homeostasis and inhibits the growth of *Staphylococcus aureus*. *Contrast Media & Molecular Imaging, 2022*, Article 8743096.
Manabe, A., Nakayama, S., & Sakamoto, K. (1987). Effects of essential oils on erythrocytes and hepatocytes from rats and dipalmitoyl phosphatidylcholine-liposomes. *Japanese Journal of Pharmacology, 44*(1), 77–84.
Manzoor, A., Dar, A. H., Kumar Pandey, V., Shams, R., Khan, S., Panesar, P. S., Kennedy, J. F., Fayaz, U., & Khan, S. A. (2022). Recent insights into polysaccharide-based hydrogels and their potential applications in food sector: A review. *International Journal of Biological Macromolecules, 213*, 987–1006.
Michalska-Sionkowska, M., Walczak, M., & Sionkowska, A. (2017). Antimicrobial activity of collagen material with thymol addition for potential application as wound dressing. *Polymer Testing, 63*, 360–366.
Motta, M. V. L., de Castro, E. V. R., Muri, E. J. B., Loureiro, B. V., Costalonga, M. L., & Filgueiras, P. R. (2019). Thermal and spectroscopic analyses of guar gum degradation submitted to turbulent flow. *International Journal of Biological Macromolecules, 131*, 43–49.
Nagoor Meeran, M. F., Javed, H., Al Taee, H., Azimullah, S., & Ojha, S. K. (2017). Pharmacological properties and molecular mechanisms of thymol: Prospects for its therapeutic potential and pharmaceutical development. *Frontiers in Pharmacology, 8*, 380.
Nemati, M. M., Heidari, R., Keshavarzi, A., Ahmadi, A., Abedi, M., Ranjbar, S., & Ghasemi, Y. (2024). In vitro and in vivo evaluation of electrospun PVA nanofiber containing ZnO/curcumin for wound healing application. *Applied Biochemistry and Biotechnology*. https://doi.org/10.1007/s12010-024-05018-x
Noach, N., Lavy, E., Reifen, R., Friedman, M., Kirmayer, D., Zelinger, E., … Reifen, E. (2023). Zinc chloride is effective as an antibiotic in biofilm prevention following septoplasty. *Scientific Reports, 13*(1), 8344.
Nostro, A., Roccaro, A. S., Bisignano, G., Marino, A., Cannatelli, M. A., Pizzimenti, F. C., … Blanco, A. R. (2007). Effects of oregano, carvacrol and thymol on *Staphylococcus aureus* and *Staphylococcus epidermidis* biofilms. *Journal of Medical Microbiology, 56*(Pt 4), 519–523.
Oliveira, T. F., Bertechini, A. G., Bricka, R. M., Kim, E. J., Gerard, P. D., & Peebles, E. D. (2015). Effects of in ovo injection of organic zinc, manganese, and copper on the hatchability and bone parameters of broiler hatchlings. *Poultry Science, 94*(10), 2488–2494.
Ozgen, M., Reese, R. N., Tulio, A. Z., Jr., Scheerens, J. C., & Miller, A. R. (2006). Modified 2,2-azino-bis-3-ethylbenzothiazoline-6-sulfonic acid (abts) method to measure antioxidant capacity of selected small fruits and comparison to ferric reducing antioxidant power (FRAP) and 2,2′-diphenyl-1-picrylhydrazyl (DPPH) methods. *Journal of Agricultural and Food Chemistry, 54*(4), 1151–1157.
Pita-Vilar, M., Concheiro, A., Alvarez-Lorenzo, C., & Diaz-Gomez, L. (2023). Recent advances in 3D printed cellulose-based wound dressings: A review on in vitro and in vivo achievements. *Carbohydrate Polymers, 321*, Article 121298.
Ponce, M. L., & Kleinmann, H. K. (2003). The chick chorioallantoic membrane as an in vivo angiogenesis model. *Current Protocols in Cell Biology, 18*(1), 19.15.11–19.15.16.
Qin, Y., Zhu, C., Chen, J., Chen, Y., & Zhang, C. (2006). The absorption and release of silver and zinc ions by chitosan fibers. *Journal of Applied Polymer Science, 101*(1), 766–771.
Rafigh, S., Soleymani, A., & Heydarinasab, A. (2021). Sulfated xanthan: Synthesis, characterization and biological evaluation. *Polymer Bulletin, 78*, 4899–4918.
Ruijssenaars, H. J., de Bont, J. A., & Hartmans, S. (1999). A pyruvated mannose-specific xanthan lyase involved in xanthan degradation by *Paenibacillus alginolyticus* XL-1. *Applied and Environmental Microbiology, 65*(6), 2446–2452.
Salesa, B., Sabater, I. S. R., & Serrano-Aroca, Á. (2021). Zinc chloride: Time-dependent cytotoxicity, proliferation and promotion of glycoprotein synthesis and antioxidant gene expression in human keratinocytes. *Biology (Basel), 10*(11).
Sandiford, N. A., Franceschini, M., & Kendoff, D. (2020). The burden of prosthetic joint infection (PJI). *Annals of Joint, 6*.
Sapkota, M., Li, L., Kim, S. W., & Soh, Y. (2018). Thymol inhibits RANKL-induced osteoclastogenesis in RAW264.7 and BMM cells and LPS-induced bone loss in mice. *Food and Chemical Toxicology, 120*, 418–429.
Schäfer, M., & Werner, S. (2008). Oxidative stress in normal and impaired wound repair. *Pharmacological Research, 58*(2), 165–171.
Schreiber, C., Ghebremedhin, M., Zielbauer, B., Dietz, N., & Vilgis, T. (2020). Interaction of xanthan gums with galacto- and glucomannans. Part I: Molecular interaction and synergism in cold gelled systems. *Journal of Physics: Materials, 3*, Article 034013.
Seijo-Rabina, A., Paramés-Estevez, S., Concheiro, A., Perez-Muñuzuri, A., & Alvarez-Lorenzo, C. (2024). Effect of wound dressing porosity and exudate viscosity on the exudate absorption: In vitro and in silico tests with 3D printed hydrogels. *International Journal of Pharmaceutics: X, 8*, Article 100288.
Shen, C., Wu, M., Sun, C., Li, J., Wu, D., Sun, C., … Chen, K. (2022). Chitosan/PCL nanofibrous films developed by SBS to encapsulate thymol/HPβCD inclusion complexes for fruit packaging. *Carbohydrate Polymers, 286*, Article 119267.
Silva, L. N., Zimmer, K. R., Macedo, A. J., & Trentin, D. S. (2016). Plant natural products targeting bacterial virulence factors. *Chemical Reviews, 116*(16), 9162–9236.
Štiglic, A. D., Gürer, F., Lackner, F., Bračič, D., Winter, A., Gradišnik, L., … Mohan, T. (2022). Organic acid cross-linked 3D printed cellulose nanocomposite bioscaffolds with controlled porosity, mechanical strength, and biocompatibility. *iScience, 25*(5), Article 104263.
Sun, C., Cao, J., Wang, Y., Chen, J., Huang, L., Zhang, H., … Sun, C. (2021). Ultrasound-mediated molecular self-assemble of thymol with 2-hydroxypropyl-β-cyclodextrin for fruit preservation. *Food Chemistry, 363*, Article 130327.
Sun, X., Lu, L., Liao, X., Zhang, L., Lin, X., Luo, X., & Ma, Q. (2018). Effect of in ovo zinc injection on the embryonic development and epigenetics-related indices of zinc-deprived broiler breeder eggs. *Biological Trace Element Research, 185*(2), 456–464.
Tacconelli, E., Carrara, E., Savoldi, A., Harbarth, S., Mendelson, M., Monnet, D. L., … Magrini, N. (2018). Discovery, research, and development of new antibiotics: The WHO priority list of antibiotic-resistant bacteria and tuberculosis. *The Lancet Infectious Diseases, 18*(3), 318–327.
Thessrimuang, N., & Prachayawarakorn, J. (2019). Characterization and properties of high amylose mung bean starch biodegradable films cross-linked with malic acid or succinic acid. *Journal of Polymers and the Environment, 27*.
Tian, L., Wang, X., Liu, R., Zhang, D., Wang, X., Sun, R., Guo, W., Yang, S., Li, H., & Gong, G. (2021). Antibacterial mechanism of thymol against *Enterobacter sakazakii*. *Food Control, 123*, Article 107716.

Tudu, M., & Samanta, A. (2023). Natural polysaccharides: Chemical properties and application in pharmaceutical formulations. *European Polymer Journal, 184*, Article 111801.

Veith, A. P., Henderson, K., Spencer, A., Sligar, A. D., & Baker, A. B. (2019). Therapeutic strategies for enhancing angiogenesis in wound healing. *Advanced Drug Delivery Reviews, 146*, 97–125.

Virzì, N. F., Diaz-Rodriguez, P., Concheiro, A., Pittalà, V., & Alvarez-Lorenzo, C. (2024). Xanthan gum/guar gum-based 3D-printed scaffolds for wound healing: Production, characterization, and biocompatibility screening. *Carbohydrate Polymer Technologies and Applications, 7*, Article 100523.

Vivero-Lopez, M., Xu, X., Muras, A., Otero, A., Concheiro, A., Gaisford, S., … Goyanes, A. (2021). Anti-biofilm multi drug-loaded 3D printed hearing aids. *Materials Science & Engineering. C, Materials for Biological Applications, 119*, Article 111606.

Walsh, D. J., Livinghouse, T., Goeres, D. M., Mettler, M., & Stewart, P. S. (2019). Antimicrobial activity of naturally occurring phenols and derivatives against biofilm and planktonic bacteria. *Frontiers in Chemistry, 7*, 653.

Yang, H., Wang, C., Liu, C., Chen, H., Wu, Y., Han, J., … Zheng, Y. (2017). Evolution of the degradation mechanism of pure zinc stent in the one-year study of rabbit abdominal aorta model. *Biomaterials, 145*, 92–105.

Yuan, N., Shao, K., Huang, S., & Chen, C. (2023). Chitosan, alginate, hyaluronic acid and other novel multifunctional hydrogel dressings for wound healing: A review. *International Journal of Biological Macromolecules, 240*, Article 124321.

Zhang, S., Sun, Y., Nie, Q., Hu, J., Li, Y., Shi, Z., Ji, H., Zhang, H., Zhao, M., Chen, C., & Nie, S. (2024). Effects of four food hydrocolloids on colitis and their regulatory effect on gut microbiota. *Carbohydrate Polymers, 323*, Article 121368.

Zhao, S., Seitz, J. M., Eifler, R., Maier, H. J., Guillory, R. J., 2nd, Earley, E. J., … Drelich, J. W. (2017). Zn-Li alloy after extrusion and drawing: Structural, mechanical characterization, and biodegradation in abdominal aorta of rat. *Materials Science & Engineering. C, Materials for Biological Applications, 76*, 301–312.